iScience

CellPress
OPEN ACCESS

Article

Modelling TGFβR and Hh pathway regulation of prognostic matrisome molecules in ovarian cancer

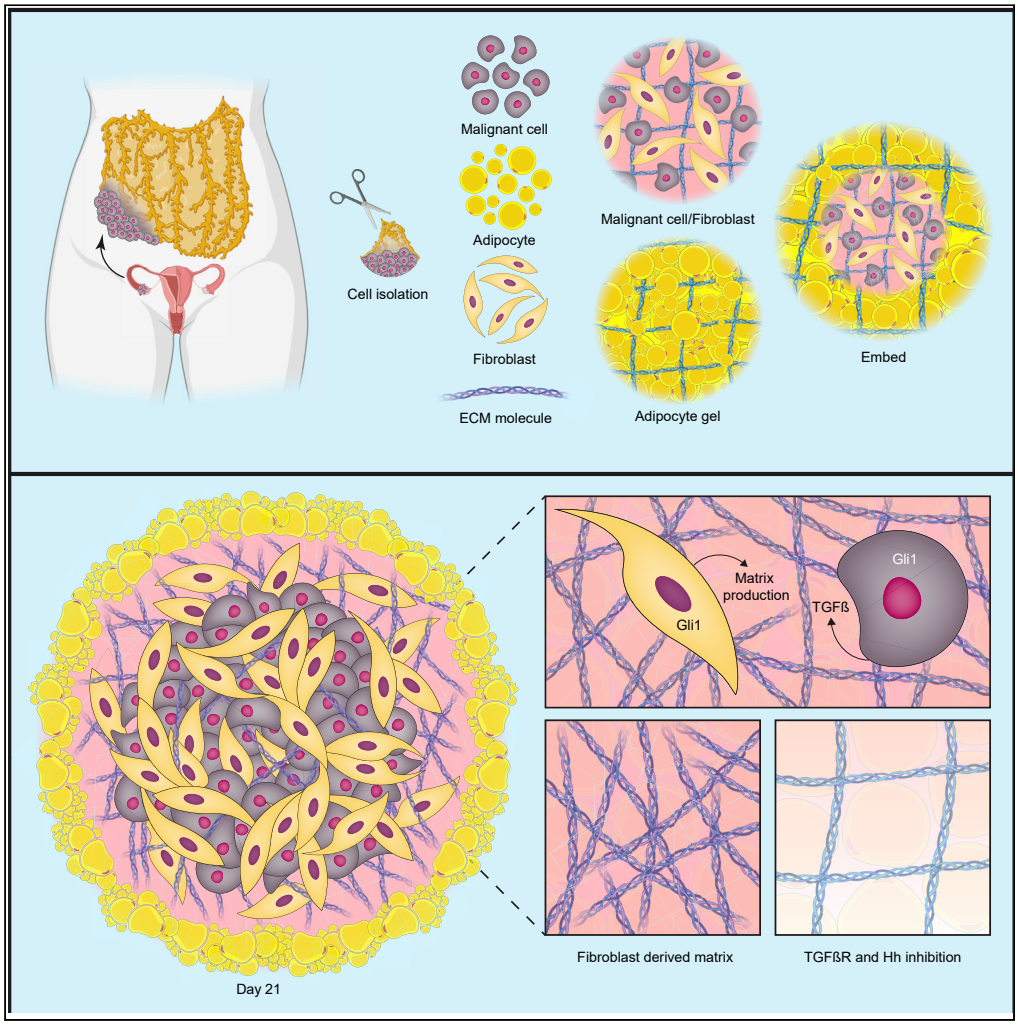

Robin M. Delaine-Smith, Eleni Maniati, Beatrice Malacrida, ..., Oliver M.T. Pearce, Martin M. Knight, Frances R. Balkwill

f.balkwill@qmul.ac.uk

Highlights

Increase in six ECM molecules in biopsies associates with poor prognosis in HGSOC

These six ECM molecules are produced in tri-cultures, predominantly by fibroblasts

TGF-β and Hedgehog pathway cross talk involved in ECM production in tri-cultures

Tri-cultures recapitulate aspects of ECM production and regulation in biopsies

Delaine-Smith et al., iScience *24*, 102674
June 25, 2021
https://doi.org/10.1016/j.isci.2021.102674

iScience

CellPress
OPEN ACCESS

Article

Modelling TGFβR and Hh pathway regulation of prognostic matrisome molecules in ovarian cancer

Robin M. Delaine-Smith,[1,2] Eleni Maniati,[1] Beatrice Malacrida,[1] Sam Nichols,[1] Reza Roozitalab,[1] Roanne R. Jones,[1] Laura S.M. Lecker,[1] Oliver M.T. Pearce,[1] Martin M. Knight,[2] and Frances R. Balkwill[1,3,*]

SUMMARY

In a multi-level "deconstruction" of omental metastases, we previously identified a prognostic matrisome gene expression signature in high-grade serous ovarian cancer (HGSOC) and twelve other malignancies. Here, our aim was to understand how six of these extracellular matrix (ECM) molecules, COL11A1, cartilage oligomeric matrix protein, FN1, versican, cathepsin B, and COL1A1, are upregulated in cancer. Using biopsies, we identified significant associations between TGFβR activity, Hedgehog (Hh) signaling, and these ECM molecules and studied the associations in mono-, co-, and tri-culture. Activated omental fibroblasts (OFs) produced more matrix than malignant cells, directed by TGFβR and Hh signaling cross talk. We "reconstructed" omental metastases in tri-cultures of HGSOC cells, OFs, and adipocytes. This combination was sufficient to generate all six ECM proteins and the matrisome expression signature. TGFβR and Hh inhibitor combinations attenuated fibroblast activation and gel and ECM remodeling in these models. The tri-culture model reproduces key features of omental metastases and allows study of diseased-associated ECM.

INTRODUCTION

Desmoplasia and extracellular matrix (ECM) remodeling are common features of human solid tumors and are driven by the continued presence of malignant cells. In high-grade serous ovarian cancer (HGSOC), there is increasing evidence that stromal components play a key role in tumor growth, promoting aggressive malignant cell phenotypes (Tothill et al., 2008; Yeung et al., 2018).

Previously, we reported a tumor-associated matrisome gene signature, the matrix index (MI), which predicted poor prognosis in patients with HGSOC and 12 other solid tumor types (Pearce et al., 2018). Six of these genes, *COL11A1*, *COMP*, *FN1*, *VCAN*, *CTSB*, and *COL1A1*, were significantly upregulated with disease and have all previously been associated with tumor progression, poor prognosis, and invasive malignant cell phenotypes in ovarian and/or other cancers (Yeung et al., 2013; Ruan et al., 2015; Englund et al., 2016) (Waalkes et al., 2010) (Jia et al., 2016). A number of signaling pathways have been linked with some of these molecules including activation of FAK, TGFβ-SMAD2/3 signaling, PDGF/PDGFR signaling, and Wnt and Hh/GLI signaling (Kenny et al., 2014; Cheon et al., 2014; Yeung et al., 2013; Erdogan et al., 2017; Vazquez-Villa et al., 2015); however, it is uncertain if there is a common regulatory mechanism that links them.

One of the key stromal cell types, the activated fibroblast, is a major producer of tumor ECM (Laklai et al., 2016; Bhowmick et al., 2004; Klingberg et al., 2013; Sahai et al., 2020). These resident or infiltrating cells acquire a phenotype most often characterized by expression of vimentin, alpha smooth muscle actin (αSMA), fibroblast activation protein (FAP), fibroblast-specific protein (FSP), or yes-associated protein (YAP) (Hanley et al., 2016; Calvo et al., 2013; Shiga et al., 2015). Previously, we reported a strong positive correlation between the density of αSMA+ and FAP+ stromal cells and the degree of disease in metastatic HGSOC [9]. Signaling pathways associated with the activation of αSMA+ fibroblasts have included, most notably, TGFβ as well as Hedgehog (Hh) [18] (Tian et al., 2009; Sahai et al., 2020; Didiasova et al., 2017).

The main goal of this study was to identify cells and signaling pathways regulating production of the six upregulated MI molecules and then build a human multi-cellular model replicating this disease process. We first characterized biopsies from human HGSOC omental metastases and used *in silico* analysis of

[1]Barts Cancer Institute, Queen Mary University of London, Charterhouse Square EC1M 6BQ, London, UK

[2]Institute of Bioengineering and School of Engineering and Materials Science, Queen Mary University of London, Mile End Road E1, London, UK

[3]Lead contact

*Correspondence: f.balkwill@qmul.ac.uk

https://doi.org/10.1016/j.isci.2021.102674

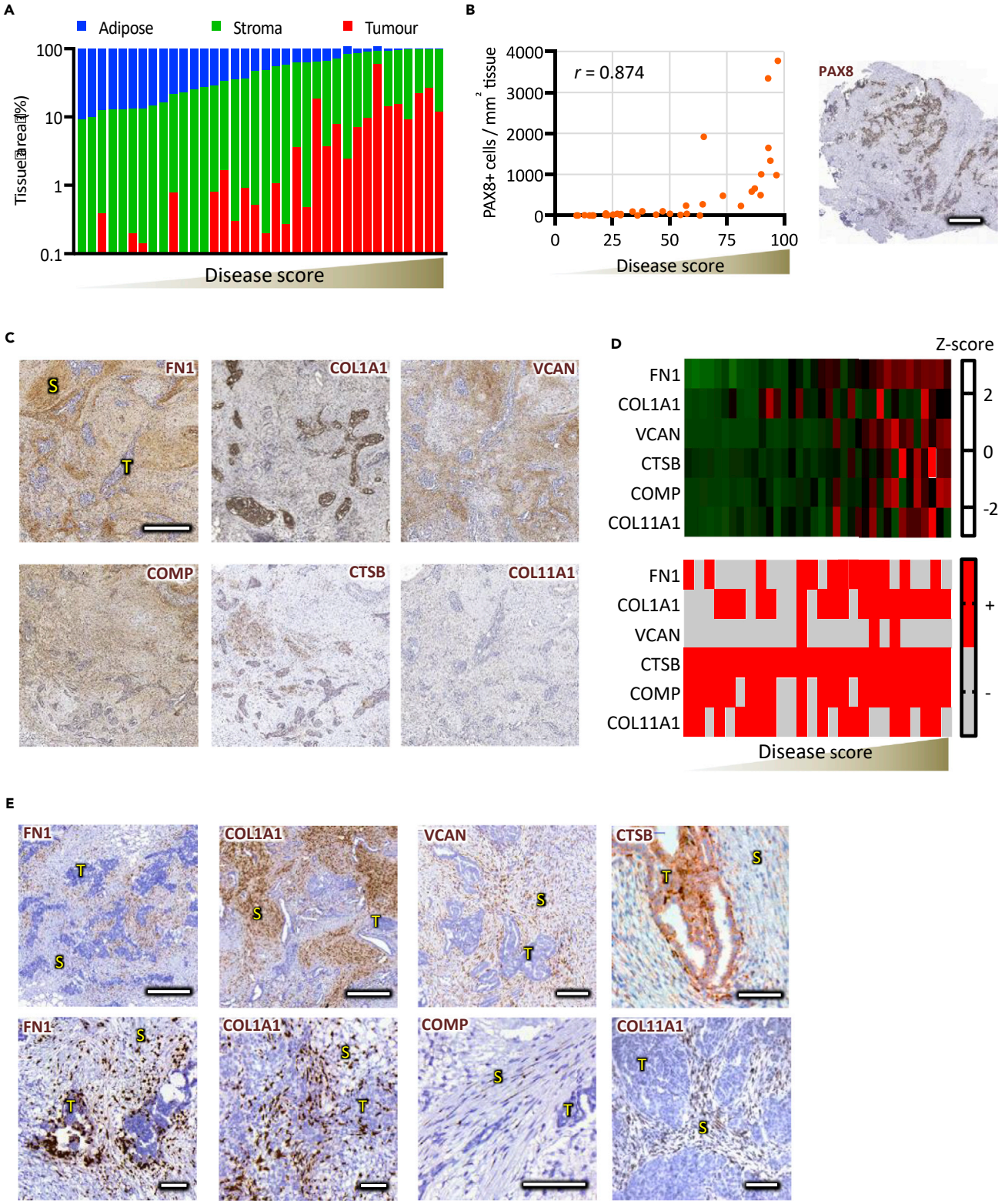

Figure 1. Tumor-matrix proteins are diversely produced by stromal and malignant cells

(A) Disease score vs. tissue area (log scale) for 36 stage 3–4 HGSOC patient omental samples correlated with (B) PAX8+ malignant cells stained via IHC. (C) IHC for FN1, COL1A1, VCAN, COMP, CTSB, and COL11A1. All showed positive correlations with disease score and heterogeneous malignant cell staining.

Figure 1. *Continued*

(D) *Z* score heatmap (top) of matrix area for all samples and a binary heatmap (bottom) display tumor positivity (red) or negativity (c) for matrix molecules.
(E) RNAscope *in situ* hybridization for the six matrix molecules (brown). Spearman's rank correlation coefficient, *r*.
In (C) and (E), S is stroma and T is tumor. Scale bars represent (B) 1000 μm, (C) 200 μm, and (E) (top row COL1A1 and FN1) 500 μm, (VCAN) 200 μm, and the rest are 100 μm.

HGSOC samples to generate hypotheses. We then isolated early passage and primary cell cultures from biopsies for validation and to build an informed novel 3D tri-culture HGSOC model. We report that TGFβR and Hh signaling are important regulators of the six upregulated MI molecules that are mainly produced by αSMA+/FAP+ omental fibroblasts (OFs) and that cross talk between these two pathways supports initiation and maintenance of this activated phenotype. Moreover, our novel human HGSOC model replicated some key features found in HGSOC omental biopsies and allowed us to understand clinically relevant regulation of diseased-associated matrisome molecules.

RESULTS

Stromal and malignant cells diversely produce disease-associated matrix molecules

We analyzed thirty-six omental biopsies with a spectrum of tissue remodeling and disease involvement, all from patients with stage 3–4 HGSOC. Tissues were assigned a disease score based on area of tissue remodeled with disease-associated stroma and malignant cells (Figure 1A) as previously described (Pearce et al., 2018). Density of PAX8+ cells, a marker of the malignant cells, correlated strongly ($r = 0.874$) with disease score, as expected (Figures 1B and S1A). All omenta studied were from patients with confirmed metastases, but malignant cells were only visible in 26 of 36 biopsies.

Matrisome protein density was measured by immunohistochemistry (IHC) in tissue sections and quantified with Definiens Tissue Suite software. Density of all six upregulated MI molecules increased significantly with disease progression (Figures 1C, 1D, and S1B). FN1 had the strongest correlation ($r = 0.969$) with disease score, had the greatest average density, and was primarily located throughout the stroma but was also found in malignant cells in 50% (13/26) of biopsies. Versican (VCAN) was largely confined to stroma with low malignant cell positivity (3/26 biopsies). Cartilage oligomeric matrix protein (COMP) was present in both stroma and most malignant cells (21/26). Cathepsin B (CTSB) was present in malignant cells of all samples with additional positivity in dense aligned stromal borders. COL11A1 was most common in stroma adjacent to malignant cells or with high cell alignment, and there was malignant cell positivity in 16 of 26 biopsies. COL1A1 had the weakest correlation with the disease score and was found heterogeneously throughout the stroma and malignant cells (18/26 biopsies). Figure 1D summarizes the pattern of malignant cell positivity for the upregulated MI molecules.

To further study origin of the upregulated MI molecules, we conducted RNAscope *in situ* hybridization on highly diseased tissue sections (Figure 1E). Consistent with IHC data, *FN1* and *COL1A1* were expressed in stroma adjacent to malignant cells and in some malignant cells. *VCAN* and *COMP* were expressed mostly in stromal cells with elongated morphology that bordered the malignant cells. A minority of malignant cells had *VCAN* expression; however, in contrast to IHC, no *COMP* expression was observed in malignant cells. *CTSB* was expressed in all malignant cells and in stroma at some malignant cell:stromal borders. *COL11A1* was expressed in stroma adjacent to malignant cells or where stromal cells appeared elongated and there was expression in some malignant cells.

In summary, these data support and extend our previous RNAseq and proteomic results in HGSOC confirming positive correlations of the upregulated MI molecules with disease score and identifying spatial location and cellular origin.

The prognostic matrisome molecules associate with TGFβ and Hh signaling

Our next aim was to identify common regulatory pathways for the six MI molecules. We first integrated protein-protein interaction and signaling pathway data from public ovarian cancer databases using PathwayLinker.org (Farkas et al., 2012). Figure 2A illustrates the interaction network of the upregulated MI molecules along with their first neighbor interactors. There was at least one direct or indirect interaction linking *FN1*, *VCAN*, *COMP*, *COL1A1*, and *CTSB*. Based on the upregulated MI molecules and their first neighbor interactors, TGFβ (Kyoto Encyclopedia of Genes and Genomes [KEGG]) signaling pathway was

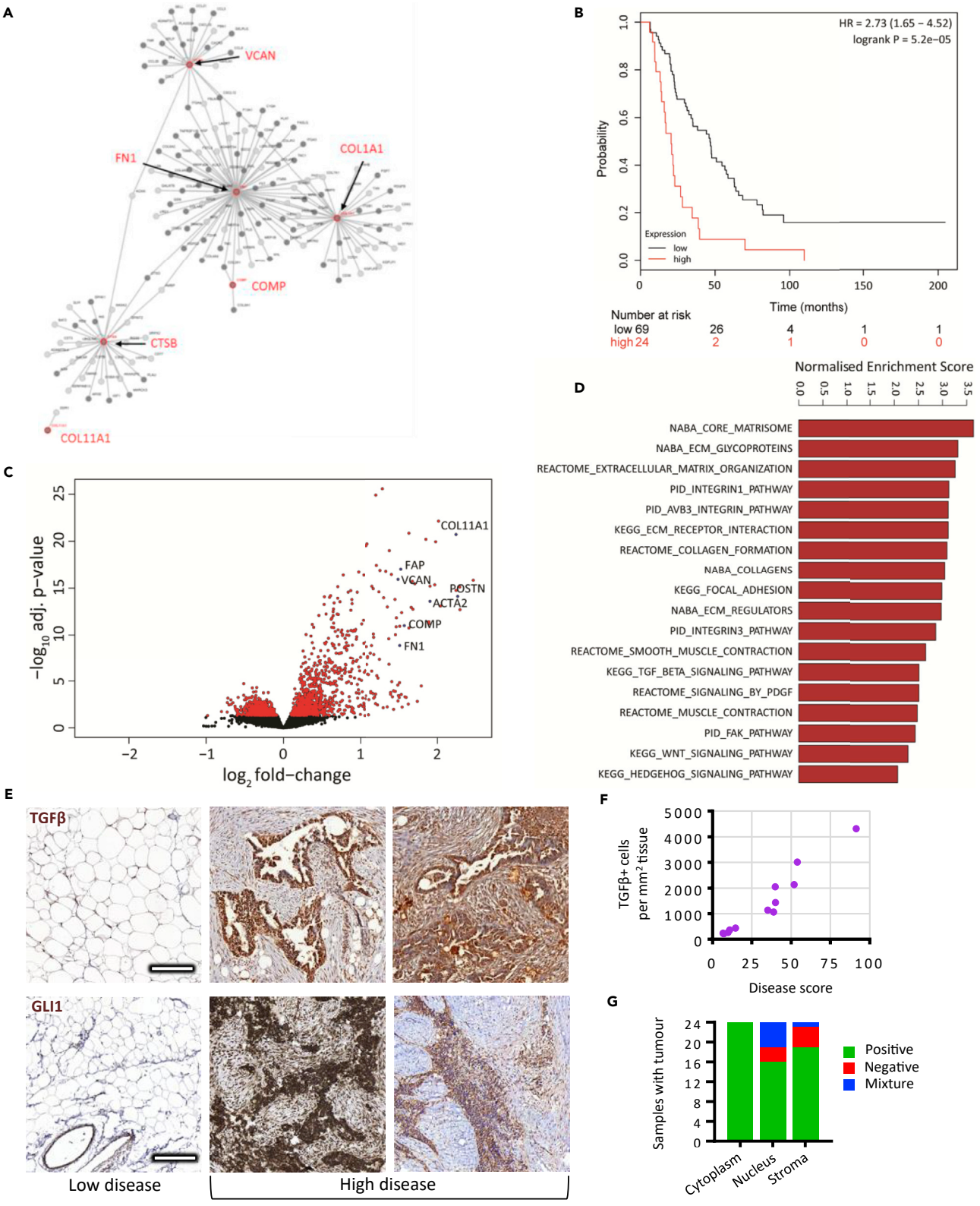
A
VCAN
FN1
COL1A1
COMP
CTSB
COL11A1
B
HR = 2.73 (1.65 – 4.52)
logrank P = 5.2e−05
Probability
Expression
low
high
Time (months)
Number at risk
low 69 26 4 1 1
high 24 2 1 0 0
C
−log10 adj. p−value
log2 fold−change
COL11A1
FAP
VCAN
POSTN
ACTA2
COMP
FN1
D
Normalised Enrichment Score
NABA_CORE_MATRISOME
NABA_ECM_GLYCOPROTEINS
REACTOME_EXTRACELLULAR_MATRIX_ORGANIZATION
PID_INTEGRIN1_PATHWAY
PID_AVB3_INTEGRIN_PATHWAY
KEGG_ECM_RECEPTOR_INTERACTION
REACTOME_COLLAGEN_FORMATION
NABA_COLLAGENS
KEGG_FOCAL_ADHESION
NABA_ECM_REGULATORS
PID_INTEGRIN3_PATHWAY
REACTOME_SMOOTH_MUSCLE_CONTRACTION
KEGG_TGF_BETA_SIGNALING_PATHWAY
REACTOME_SIGNALING_BY_PDGF
REACTOME_MUSCLE_CONTRACTION
PID_FAK_PATHWAY
KEGG_WNT_SIGNALING_PATHWAY
KEGG_HEDGEHOG_SIGNALING_PATHWAY
E
TGFβ
GLI1
Low disease
High disease
F
TGFβ+ cells per mm² tissue
Disease score
G
Samples with tumour
Positive
Negative
Mixture
Cytoplasm
Nucleus
Stroma

Figure 2. The six upregulated matrix index molecules (FN1, COL1A1, VCAN, COMP, CTSB, COL11A1) associate with TGFβ and Hh signaling

(A) Interaction network diagram obtained on PathwayLinker.org for the six upregulated matrix index molecules.

(B) Kaplan-Meier survival curve with overall survival from the International Cancer Genome Consortium ovarian data set divided by high or low average gene expression of the six matrix index molecules. The x axis is in the unit of months.

(C) Volcano plot displays comparison of gene expression between high and low groups, highlighting significant upregulation of matrix molecules and stromal activation markers in the high group. Red dots indicate adjusted P value <0.05.

(D) Plot of normalized enrichment score (NES) obtained from GSEA highlights over-expressed pathways in the high group compared with the low group, including TGFβ and Hh signaling (false discovery rate, FDR <0.05).

(E) IHC for TGFβ and GLI1 was performed on biopsies.

(F) TGFβ IHC was quantified as the number of positive cells in stained tissue.

(G) Samples with malignant cells were identified for populations with GLI1 positivity, negativity, or a mixture of both in malignant cell cytoplasm and nuclei, as well as stromal cells. Scale bars represent 200 μm.

significantly overrepresented ($p = 2.2 \times 10^{-9}$), along with ECM (KEGG), platelet-derived growth factor (PDGF) (Reactome), actin (KEGG), and P53 (KEGG) (Table S1).

We next interrogated the International Cancer Genome Consortium transcriptional data set of HGSOC biopsies (Patch et al., 2015) looking at association between prognosis and mean expression levels of upregulated MI genes. We found that high average expression of upregulated MI genes associated with significantly worse survival in HGSOC (log rank $P = 5.2 \times 10^{-5}$) (Figure 2B). Differentially expressed genes in the high expression group included periostin, several collagens, osteonectin, and activation markers *ACTA2* and *FAP* (Figure 2C). Gene set enrichment analysis (GSEA) highlighted over-expression of matrisome, ECM, collagen, focal adhesion, and smooth muscle contraction pathways (Figure 2D). Of particular interest was significant enrichment for TGFβ (KEGG), WNT (KEGG), PDGF (Reactome), and Hh (KEGG) signaling (Figure 2D and Table S2). These results suggested that at least five of the upregulated MI molecules might be co-regulated in HGSOC and that TGFβ signaling is involved.

To investigate this further, we stained tissue sections for TGFβ (Figure 2E) and found a strong correlation between positive cell density and disease score (Figure 2F), observing the strongest staining in malignant cells. We also stained tissues for GLI1 (Figure 2E), a main downstream target of Hh signaling, which has been previously associated with collagen-producing αSMA+ phenotypes (Sahai et al., 2020; Tian et al., 2009) and also implicated in TGFβ cross-talk-promoting fibrosis (Didiasova et al., 2017; Javelaud et al., 2012). Tissues with a high disease score had significant GLI1 positivity in contrast to tissues with low disease scores that had relatively little. Malignant cells in all biopsies displayed cytoplasmic GLI1, but nuclear GLI1 varied; 16 of 26 biopsies had total nuclear positivity, four of 26 were totally nuclear negative, and six of 26 were mixed (Figure 2G). GLI1+ stromal cells were identified in 22 of 26 malignant cell biopsies displaying a mixture of cytoplasmic and nuclear positivity.

Malignant cells upregulate TGFβ3 and heterogeneously express matrisome molecules

Our next aim was to build 2D and 3D *in vitro* human cell models to allow us to validate and extend our findings. First, we investigated two HGSOC malignant cell lines for suitability in such models. G164 was established in our lab from patients with omental metastases and kept at a low passage number. AOCS1 was also established from a patient with HGSOC and kept at a low passage number. Both cell lines showed genetic changes characteristic of HGSOC (Tamura et al., 2020). The original tissue biopsies for both cell lines showed malignant cell PAX8 positivity and cell lines cultured *in vitro* maintained PAX8 nuclear positivity (Figure 3A). We characterized these HGSOC cells by RNA sequencing. Unsupervised clustering using principal component analysis (PCA) illustrated significant transcriptional differences between the two cell lines with the first principle component accounting for more than 89% of the difference (Figure 3B). However, within the same cell line, there was relatively little variation between monolayer and spheroid culture. GSEA highlighted significant canonical pathway differences between the two cell lines; notably, AOCS1 had enriched Hh-GLI signaling, and G164 was enriched in transcriptional activity of SMAD2/3/4 and signaling by TGFβR complex (Figure 3C). The differences in Hh signaling between AOCS1 and G164 were confirmed by analyzing GLI1 expression using qRT-PCR (Figure 3D) and immunoflourescence (IF) (Figure 3E). In addition, cell proliferation, which Hh is known to affect, was significantly reduced in AOCS1 with a GLI1/2 inhibitor, GANT61 (Thompson et al., 2015), (Figures S2A–S2C) but not in G164 (Figure S2D). The use of a TGFβR inhibitor, SB431542 (Avgustinova et al., 2016), on the G164 cell line attenuated cell contraction of gels and also cell migration (Figures S2E and S2F), both processes associated with activated TGFβR signaling, but did not affect viability (Figure S2G). RNA sequencing and qRT-PCR detected five of the

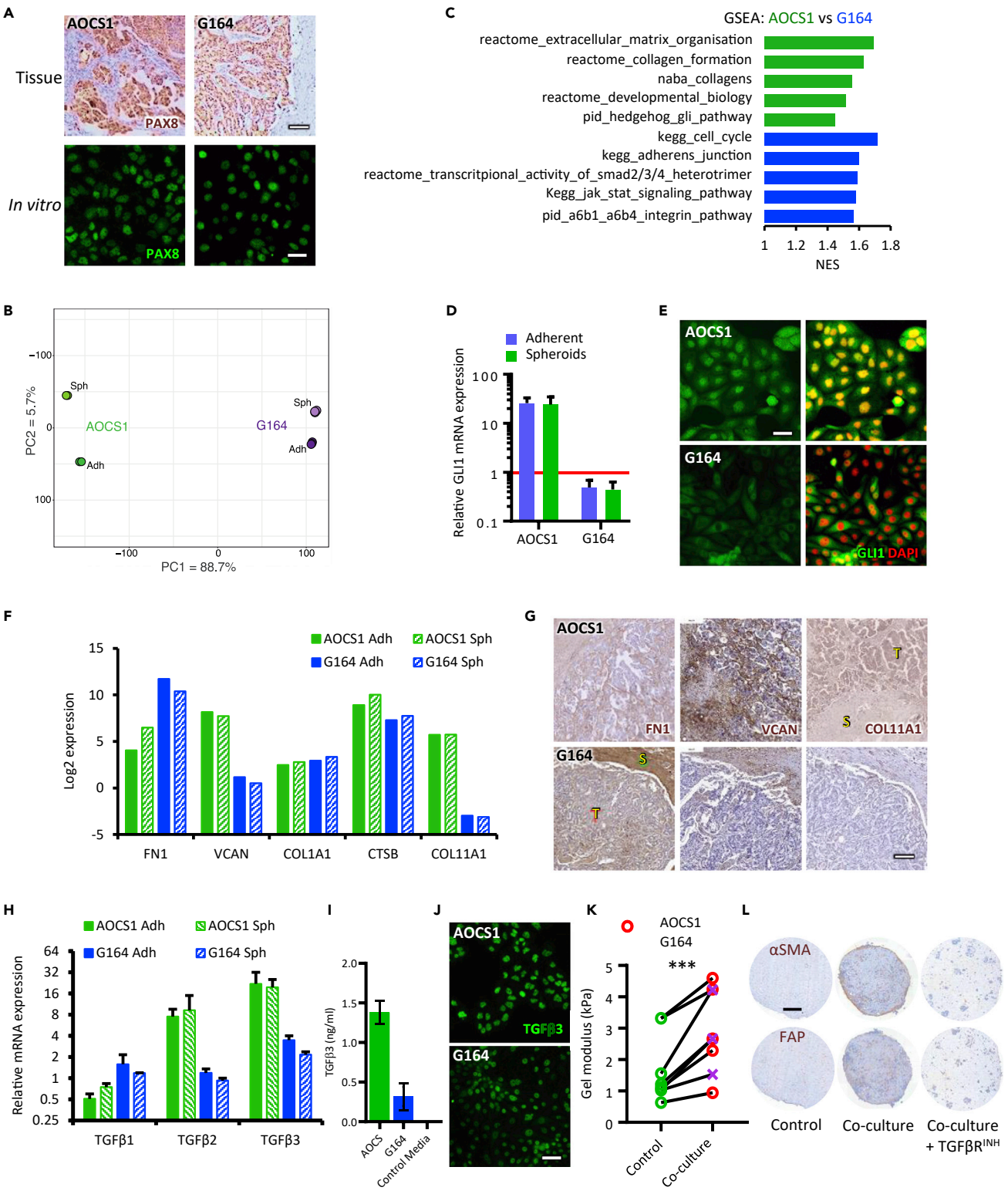

Figure 3. HGSOC malignant cells have heterogeneous signaling but all secrete TGFβ

(A) To identify malignant cells, HGSOC tissue sections and cells expanded *in vitro* were stained for PAX8 via IHC or IF, respectively.

(B) RNA sequencing was performed on AOCS1 and G164 malignant cell lines (N = 2) for adherent (Adh) and spheroid (Sph) cultures, and transcriptomic expression was analyzed using PCA.

Figure 3. *Continued*

(C) GSEA was performed on transcriptomic data, and normalized enrichment scores for AOCS1 (green) vs G164 (blue) are illustrated ($p < 0.1$).

(D–G) (D) qRT-PCR was performed for GLI1 on AOCS1 and G164; bar plot illustrates relative expression levels of GLI1 normalized to expression in normal fallopian tube cells, FT318-WT (red line) (E) GLI1 IF, (F) RNASeq log2RPKM gene expression of matrix molecules in AOCS1 and G164 cultures (COMP not detected), and (G) IHC of human biopsy sections from patients AOCS1 and G164 for FN1, VCAN, and COL11A1.

(H) TGFβ expression via qRT-PCR for malignant cells *in vitro* (N = 3), normalized to FT318-WT expression and (I) TGFβ3 released by AOCS and G164 cells after 48 h of culture.

(J) IF images of TGFβ3.

(K and L) OFs were cultured in 3D COL1 gels alone (control) or with (co-culture) AOCS1 or G164 cells for 7–14 days with or without $TGF\beta R^{INH}$ and then (K) compressed to determine gel modulus (D7); each point represents mean of 2–4 gels (n = 2–4) per OF donor (N = 8), $p < 0.001$ (two-way, paired t test) and (L) IHC (D14) performed on fixed sections of AOCS1 co-cultures for αSMA and FAP. Scale bars (A [bottom], E, J) are 50 μm and (A [top], G, L) are 250 μm.

six upregulated MI molecules (mRNA for COMP was not present) in the cell lines, but expression was heterogeneous (Figures 3F and S2H). We stained biopsy sections for differentially expressed matrix molecules identifying malignant cell positivity for COL11A1 and VCAN in AOCS1 and FN1 in G164 (Figure 3G). IF on *in vitro* monocultures displayed strong intracellular COL11A1 staining organized into fibrils in AOCS1 and significant deposition of FN1 by G164s (Figure S2I) replicating tissue staining.

Expression of the three TGFβ isoforms was analyzed in malignant cells and compared to a non-malignant cell control, wild-type immortalized FT318 fallopian tube surface epithelial cells (Figure 3H). Malignant cells expressed all three TGFβ isoforms with little difference between adherent and spheroid cultures, but TGFβ3 was the most highly expressed relative to FT318. TGFβ3 protein was also present intra-cellularly and secreted by both cell lines, as shown in the IF and enzyme-linked immunosorbent assays (Figures 3I and 3J). To test the influence of malignant cell-secreted TGFβ on fibroblast activation, we co-cultured malignant cells with primary OFs in collagen gels. All co-culture gels had a significantly greater gel modulus (stiffness) compared with respective fibroblast controls (Figure 3K), while malignant cells grown alone did not alter gel modulus (Figure S2J). In co-cultures, αSMA, FAP, and eosin staining were all increased in OFs, but expression was attenuated using the TGFBR inhibitor (Figures 3L and S2K). Interestingly, we were unable to detect expression of any Hh ligands in either cell line.

These results highlight heterogeneity in cell signaling and matrisome expression in HGSOC malignant cells, but they also reveal a commonality in upregulation of TGFβ, which activates OFs via TGFβR signaling.

TGFβ3 stimulates activation, GLI1 expression, and diseased-matrix production in omental fibroblasts

Having identified TGFβ as a stimulator of fibroblast activation, we next looked at associations between fibroblasts and malignant cells in HGSOC omental biopsies. Density of αSMA+ or FAP+ cells correlated with density of PAX8+ malignant cells ($r = 0.833$ and $r = 0.814$, respectively) (Figure 4A), and staining was highest in stroma adjacent to malignant cells (Figure S3A). We pseudo colored and overlaid consecutive αSMA and FAP tissue images (Figure 4B) identifying a αSMA+/FAP+ stromal phenotype located primarily at malignant cell borders where the densest matrix and GLI1 staining were previously seen.

When we isolated OFs from HGSOC omental biopsies, we observed a range of activation states in culture, which we categorized before use in experiments as either low (L-OFs) or high (H-OFs), defined by cell morphology and level of expression of F-actin and αSMA stress fibers (Figure S3B). Regardless of initial activation state, treating OFs with TGFβ3 increased *ACTA2* and *FAP* mRNA expression on average 4-fold and 2-fold, respectively (Figure 4C), increased IF staining for both proteins (Figures 4D and S3C) as well as the proportion of αSMA+/FAP+ cells (Figure S3D). TGFβ3 treatment also promoted F-actin fiber formation and FSP and YAP nuclear expression (Figure S3E) in L-OFs, although differences in the latter two appeared small. In Figure 2E, we identified GLI1-positive stromal cells in HGSOC tissue. Hh activation can promote collagen-producing myofibroblasts in some fibrotic diseases (Horn et al., 2012), and recently, αSMA+/GLI1+ mesenchymal cells have been identified (Schneider et al., 2018). TGFβ3-treated OFs had on average a 2.5-fold increase in GLI1 expression and a 2-fold decrease in GLI3 expression, typically considered a Hh pathway repressor (Wang et al., 2000), while SB431542 reversed this trend (Figure 4E). GLI1 IF showed weak cytoplasmic staining in L-OFs while TGFβ3-treated L-OFs had stronger cytoplasmic and positive nuclear staining (Figure 4F).

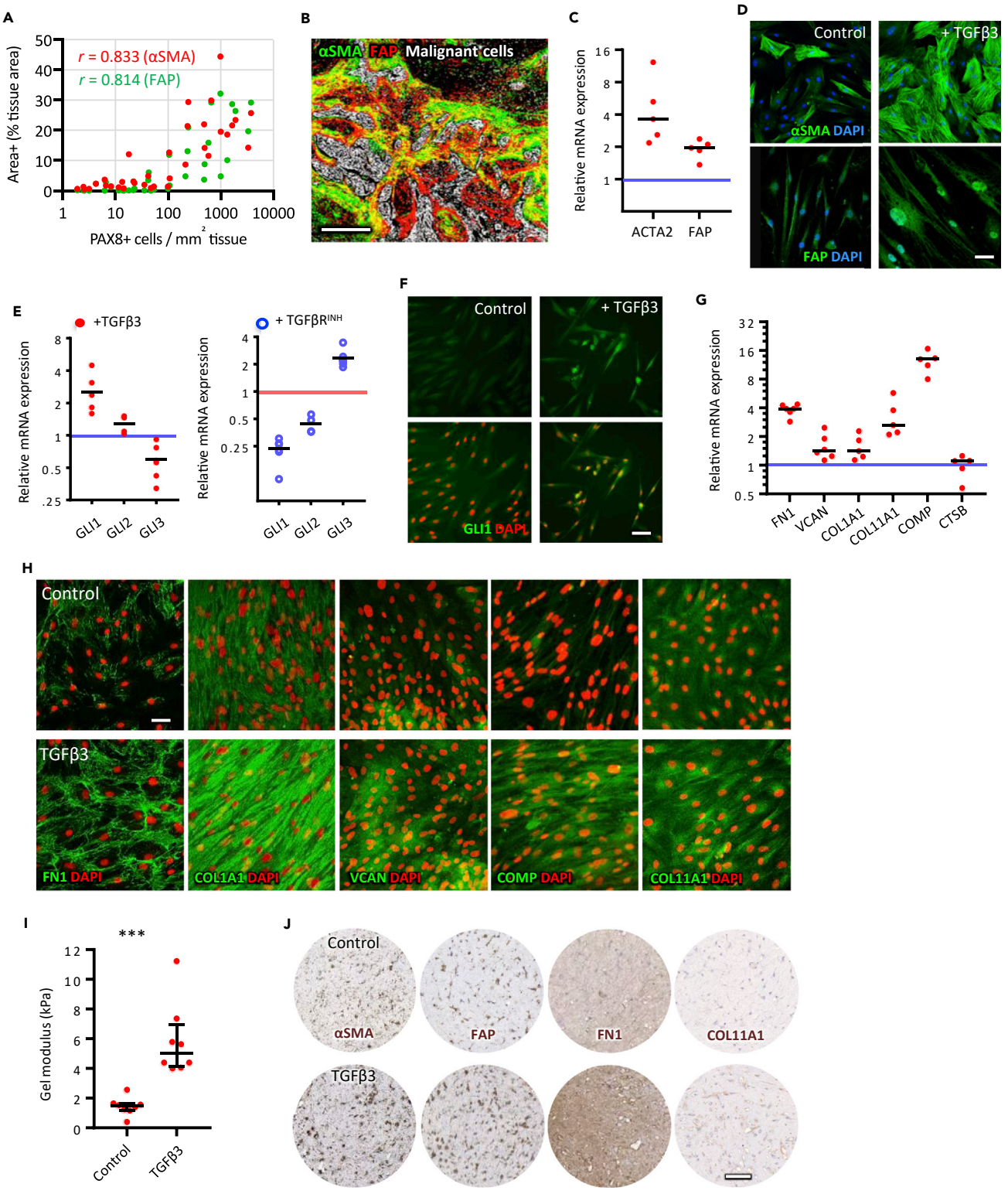

Figure 4. TGFβ3 stimulates αSMA, FAP, and GLI1 expression and tumor-matrix production in omental fibroblasts

(A) IHC identified FAP or αSMA-positive cells; both correlated positively with PAX8+ cell density.

(B) IHC images of FAP and αSMA were pseudo colored and overlaid using ImageJ to highlight double-positive cells (yellow).

Figure 4. *Continued*

(C and D) (C) TGFβ3 treatment of L-OFs caused upregulation in ACTA2 and FAP mRNA, measured by qRT-PCR, across five donors (n = 3, N = 5) and (D) increased αSMA and FAP IF.

(E) GLI1 mRNA expression was upregulated in TGFβ3-treated L-OFs (5 donors) and downregulated with SB431542 ($TGF\beta R^{INH}$) (4 donors).

(F) IF GLI1 staining shows representative images of TGFβ3-treated and untreated L-OFs.

(G) Five of the six matrix molecules were upregulated in TGFβ3-treated L-OFs at mRNA level.

(H) Representative IF staining for the five upregulated molecules.

(I and J) L-OFs were cultured in COL1 gels for seven days; TGFβ3 treatment increased (I) gel modulus (n = 2–3, N = 3, two-way t test, $p < 0.001$) and (J) expression of αSMA, FAP, FN1, and COL11A1 visualized via IHC.

Scale bars are (B) 200 μm and (D, F, and H) 50 μm and (I) 500 μm. Blue and red lines represent control (no TGFβ3 or no $TGF\beta R^{INH}$, respectively) expression.

Next, we analyzed expression of upregulated MI molecules in L-OFs and found that TGFβ3 upregulated mRNA expression of *FN1*, *VCAN*, *COL1A1*, *COL11A1*, and *COMP* (Figure 4G) and promoted matrix deposition and organization (Figure 4H). Initially, there was little VCAN or COMP in confluent untreated L-OFs but TGFβ3 induced widespread deposition of both proteins. Treated cells contained denser FN1, COL1A1, and COL11A1 fibers with greater alignment. Of particular note, COL11A1 was organized into intracellular fibers similar in appearance to microtubules.

Tissue stiffening and contraction occurs during remodeling in fibrosis-associated diseases and is caused largely by myofibroblasts (Desmouliere et al., 2005; Avgustinova et al., 2016). When we cultured L-OFs in 3D collagen gels for 7 days, TGFβ3 treatment caused ~ 4-fold increase in gel modulus compared with untreated gels (Figure 4I). Gels seeded with H-OFs formed stiffer gels than L-OFs, but modulus was significantly reduced when treated with SB431542 (Figure S3F). Cells in TGFβ3-treated gels had denser αSMA, FAP, FN1, and COL11A1 staining compared with controls (Figure 4J).

Collectively, these experiments showed that TGFβ3 promotes a αSMA+/FAP+ contractile OF phenotype associated with an upregulation of GLI1 and increased deposition of five of the six upregulated MI molecules.

TGFβR and GLI1/2 inhibitors downregulate αSMA, GLI1, and matrix molecules in OFs

We next asked if GLI1 played a downstream role in TGFβR pathway activation in H-OFs (Figure 5) and TGFb3-activated L-OFs (Figure S4). Inhibitors of TGFBRI, SB431542 (Thompson et al., 2015) or Gli1/2, GANT61 (Avgustinova et al., 2016), both reduced αSMA stress fibers in H-OFs and induced a morphology shift from a relatively large spread cell to a smaller fusiform cell (Figure 5A). Both inhibitors reduced *ACTA2* expression between 4 and 5 fold, but there was less effect on FAP (Figures 5B and S4A). Combination treatment of the inhibitors caused a synergistic effect on *ACTA2* resulting in >10-fold downregulation. Both inhibitors decreased the proportion of αSMA+/FAP+ cells with the greatest effect induced by the inhibitor combination (Figures 5C and S4B). IF confirmed αSMA stress fibers decreased with inhibitor combination, while again there was less effect on FAP (Figure 5D). Both inhibitors downregulated GLI1 3–5 fold and upregulated GLI3 2–3 fold (Figures 5E and S4C), while IF showed reduced cytoplasmic and nuclear GLI1 in H-OFs treated with the inhibitor combination (Figure 5F).

SB431542 reduced *FN1*, *VCAN*, *COL1A1*, *COMP*, and *COLL11A1* mRNA while GANT61 reduced *COL1A1*, *COMP*, and *COL11A1* (Figures 5G and S4D), implying that FN1 and VCAN are not regulated by Hh. Overall, the inhibitor combination was most effective at downregulating collagen matrix mRNA than each individual inhibitor. Figure 5H shows representative IF in 2D H-OF cultures for the five molecules downregulated at mRNA-level molecules, confirming that the effect of the inhibitor combination is replicated at the protein level. There was almost complete absence of VCAN and COMP; fibers of FN1 and COL1A1 were less and disrupted; and COL11A1 had lost fibrous structure. When H-OFs were grown in 3D collagen gels, the inhibitor combination reduced density of αSMA, FAP, FN1, and COL11A1 (Figure 5I). In contrast to OFs, there was relatively little inhibitor effect on matrix expression or organization in AOCS1 malignant cells (Figures S5A and S5B). However, in G164 malignant cells, there was a significant effect of the TGFβR inhibitor on FN1 mRNA and protein (Figures S5C and S5D), following the trend seen in OFs, and this translated to 3D cultures whereby spheroid growth was also reduced (Figure S5E). In addition, we observed a marked reduction in *TGFβ2* and *TGFβ3* expression in AOCS1 with Hh inhibitor GANT61 and a 10-fold reduction in *TGFβ2* expression in G164 with TGFBR inhibitor SB431542 (Figures S5F and S5G).

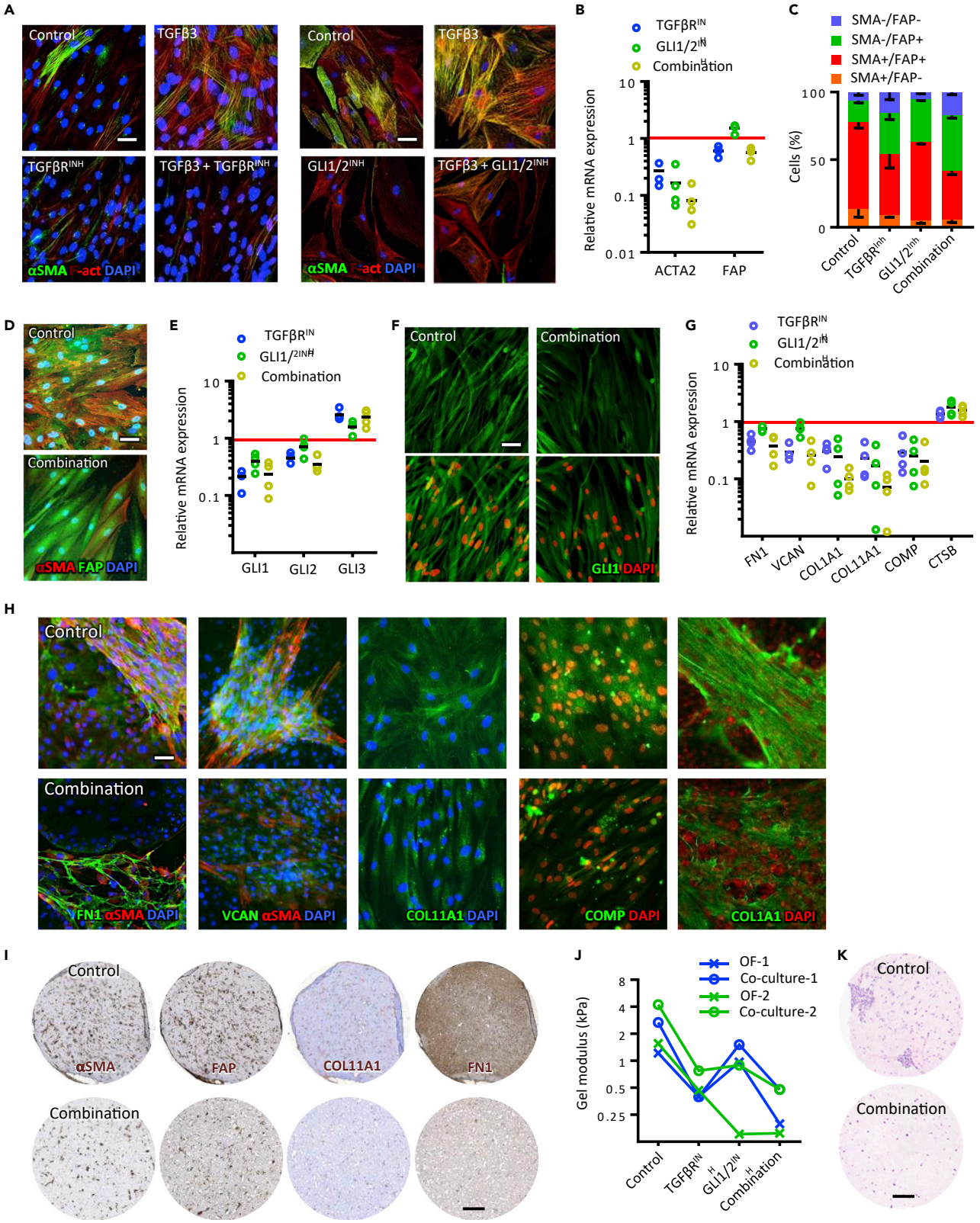
A
Control
TGFβ3
TGFβR^INH
TGFβ3 + TGFβR^INH
GLI1/2^INH
TGFβ3 + GLI1/2^INH
αSMA F-act DAPI
B
TGFβR^IN
GLI1/2^IN
Combination
Relative mRNA expression
ACTA2
FAP
C
SMA-/FAP-
SMA-/FAP+
SMA+/FAP+
SMA+/FAP-
Cells (%)
D
αSMA FAP DAPI
E
GLI1
GLI2
GLI3
F
GLI1 DAPI
G
FN1
VCAN
COL1A1
COL11A1
COMP
CTSB
H
FN1 αSMA DAPI
VCAN αSMA DAPI
COL11A1 DAPI
COMP DAPI
COL1A1 DAPI
I
αSMA
FAP
COL11A1
FN1
J
OF-1
Co-culture-1
OF-2
Co-culture-2
Gel modulus (kPa)
K

Figure 5. TGFβR and GLI1/2 inhibitors downregulate αSMA, GLI1, and tumor matrix in OFs

(A) IF for αSMA and F-actin in L-OFs treated with TGFβ3 ± TGFβR^{Inh} (SB431542) or ± GLI1/2 (GANT61) inhibitors.

(B-K) OFs with high activation (H-OFs) were treated with TGFβR^{Inh} or GLI1/2^{Inh} or combination; (B) gene expression was measured by qRT-PCR for ACTA2 and FAP (N = 4 donors). (C) Cells were analyzed via flow cytometry for percentage of cells αSMA+ and/or FAP+. (D) Activated OFs were visualized via IF for αSMA and FAP ± inhibitor combination. (E) GLI1/2/3 mRNA expression analyzed via qRT-PCR for OFs and (F) GLI1 visualized via IF in activated OFs or with combination. (G) mRNA expression of matrix molecules were analyzed via qRT-PCR for treated or untreated OFs (n = 4 donors). (H) IF visualized FN1, VCAN, COL11A1, COMP and COL1A1, and αSMA in activated OFs with or without combination. (I) IHC of control and combination-treated OF gels for αSMA, FAP, COL11A1, and FN1.

(J–K) OF-only gels or AOCS1 co-cultures were grown for 7 days with or without inhibitors and (J) gel modulus was measured (mean of 3 gels per donor, N = 2) and (K) fixed sections stained for H&E.

Scale bars (A, D, F, and H) are 50 μm and (I and K) are 500. Red lines represent control (no TGFβR^{INH}) expression.

We next co-cultured malignant cells with OFs in 3D gels and measured inhibitor effect on gel modulus. Co-cultures treated with inhibitor alone had decreased modulus, and, overall, the combination was the most effective (Figure 5J), also reducing the size of cell clusters in the gels (Figure 5K). Viability of co-cultures was unaffected by inhibitors (Figure S5H).

In summary, we found that TGFβ stimulates GLI1 promoting a αSMA COL1A1/COL11A1/COMP-rich matrix; however, Hh signaling appeared to have little involvement with VCAN or FN1 production. We also observed a synergy with TGFβR and GLI1 inhibition resulting in the inhibitor combination being most effective in attenuating activation, contraction, and matrix production. There were also regulatory differences in the two pathways between malignant cells and OFs.

A novel 3D tri-culture replicates some key features found in HGSOC biopsies

In order to conduct pre-clinical studies of therapies that could target the poor prognostic MI molecules, we require human 3D models that recreate more of the complexity and interactions in the tumor microenvironment. Adipocytes are the major cell type in the normal omentum and act as a source of energy for developing metastases (Nieman et al., 2011). We hypothesized that adipocytes could provide a relevant biological substrate for long-term malignant cell and fibroblast co-culture allowing for the study of matrisome molecule regulation and also that such tri-cultures would more closely resemble the omental tumor microenvironment.

We isolated mature adipocytes from omental digests (Figure 6A) and confirmed there were viable unilocular cells. We seeded adipocytes into low-weight (0.1w%) COL1 gels in 96-well plates, enabling adipocytes to rise up forming a compact mm-sized layer (Figure 6B). Figure 6C shows hematoxylin and eosin (H&E) images of an adipocyte gel after 14 days of culture compared to the normal human omentum. We assessed viability and perilipin-1, a marker of mature adipocytes, over 21 days. Although there appeared to be some decline in viability/live stain, there was very little dead staining at day 21 (Figure 6D), and perilipin-A levels remained relatively constant (Figure 6E). IHC for MI molecules revealed low levels of MI molecules in the adipocyte cultures (Figure S6A).

To establish tri-cultures, we inserted seven-day co-cultures (providing time for gel remodeling) directly into the middle of adipocyte gels and then incubated for a further 14 days in free-swelling conditions (Figure 6F). This time period was sufficient for remodeling of the adipose tissue and generation of cell markers and all upregulated MI molecules (Figures 6G, 6H, and S6B). PAX8 staining identified malignant cells, while FAP and αSMA staining identified activated fibroblasts located mainly at borders between malignant cells and remodeled adipose tissue (Figure 6H) as we had observed in biopsies. Both malignant cells and stromal cells were proliferating at 21 days as demonstrated by Ki67 staining (Figure 6H). Malignant cells were positive for TGFβ, and GLI1 positivity was present in malignant and stromal cells. All six upregulated MI molecules were found in the stroma and some in malignant cells (Figure 6H). We conclude that tri-cultures support malignant cell and fibroblast growth and replicate some of the key features that we have found in patient biopsies.

To further confirm that the tri-cultures were a valid model to study regulation of MI molecules and that the addition of adipocytes better replicated the human omental tumour microenvironment (TME), we conducted RNAseq analysis of the adipocyte gels, G164-OF collagen gel co-cultures, and the G164 tri-cultures (Figure 7A–7D). The tri-cultures had the most complex matrisome gene transcription signature (Figure 7A) and

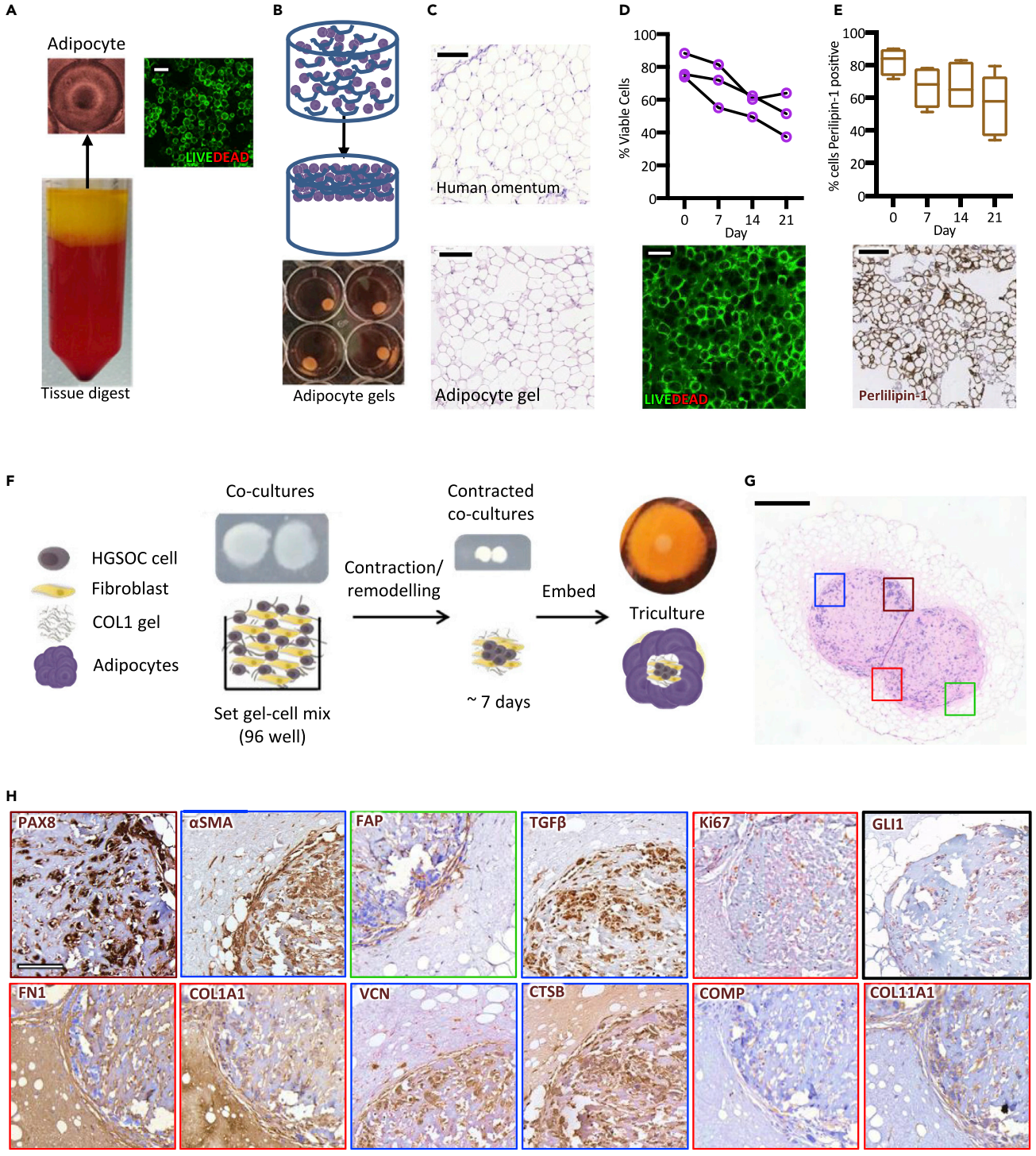

Figure 6. Omental adipocytes provide a physiological substrate for an HGSOC tri-culture model

(A) Fatty layer on top of the omental digest supernatant contains viable adipocytes, assessed by IF LIVE/DEAD assay.

(B) Adipocytes are mixed with collagen gel solution (0.1w%), seeded into 96-well plates, left 5 min at RT allowing cells to float upwards, before incubating at 37^{O}C for 45min, after which gels can be carefully handled (gels transferred to 24-well plates).

(C) H&E gel sections have similar appearance to the normal omentum.

(D and E) Adipocyte gels tested for viability via IF LIVE/DEAD assay and sectioned and stained via IHC for perilipin-1 (days 0, 7, 14, and 21); data are (D) mean of 3–5 images per donor (N = 3) and (E) median with interquartile range (N = 5).

Figure 6. *Continued*

(F) Schematic shows constituents and cells used to assemble and grow tri-cultures.

(G and H) AOCS1 tri-cultures grown for 21 days and then fixed, sectioned, and stained for H&E and via IHC; colored squares in (G) mark location of colored borders for IHC (H).

Scale bars (A, C, and D) are 100 μm, (E and H) are 200 μm, (G) and 500 μm.

showed a significant enhancement of ECM, adhesion, collagen fibril organization, and also cell migration signatures compared to the G164-OF co-cultures (Figure 7B and Table S3). Twenty-one of the 22 MI molecules originally identified by us in HGSOC omental metastases (Pearce et al., 2018) could be sufficiently detected by RNAseq, allowing us to calculate the MI of adipocyte-only gels, G164-OF cultures, and tri-cultures. Tri-cultures had an increased MI compared with adipocyte-only gels and co-cultures (Figure 7C) with values similar to diseased omental metastases from patients with HGSOC (Pearce et al., 2018). The cluster dendrogram also shows a clear separation between adipocyte cultures, co-cultures, and tri-cultures (Figure 7D).

TGFβRI and GLI1/2 inhibitor combination reduces matrisome production in tri-cultures

Having shown that MI levels were comparable to the biopsies and implicating TGFβR and Hh signaling in regulation of the upregulated MI molecules, we tested their inhibitors in the tri-cultures. We used the inhibitor combination as we saw previously that it was most effective at reducing OF activation and matrisome molecules. The inhibitor combination did not affect total cell viability (Figure S7A) but significantly reduced adipocyte gel contraction in all tri-cultures (Figures 7E and S7B) and reduced remodeling or malignant cell invasion of adipocytes (Figure S7C). Confocal microscopy showed a noticeable reduction in all six upregulated MI molecules imaged in tri-cultures treated with the inhibitor combination (Figures 7F and S7D). In controls, G164 cells formed large colonies surrounded by activated fibroblasts, but with the inhibitor combination, malignant colonies were significantly smaller and widely dispersed. In treated AOCS1 tri-cultures, matrix molecules and activation markers were also reduced and compared with controls (Figures 7F and S7D).

We also conducted RNAseq on G164 tri-cultures with the inhibitor combination. Unsupervised clustering of the data showed that the inhibitor-treated cultures segregated separately from the control tri-cultures (Figure S7E). Expression levels of fibroblast activation markers and the six upregulated MI molecules, including *CTSB*, were significantly reduced by the inhibitor combination (Figure 7G). GSEA showed significant downregulation of pathways associated with matrisome, ECM, collagens, as well as TGFβ and Hh signaling (Figures S7F, S7G, and 7H and Table S4). The overall MI was reduced to the level of the adipocyte gels or co-cultures (Figure 7I).

These experiments demonstrate that this novel tri-culture model replicates key features of the omental HGSOC tumor microenvironment, especially matrisome components from the MI signature. Moreover, we can use this model to investigate regulation of tumor-associated components.

DISCUSSION

We recently published a multi-level analysis of developing HGSOC metastases (Pearce et al., 2018). One of the significant findings was a pattern of 22 matrisome genes which we termed the MI that significantly changed with disease progression and was highly prognostic in ovarian and twelve other solid human cancers. Six of these molecules were significantly upregulated with disease progression and sixteen downregulated. In the present work, we have shown that expression levels of the six upregulated MI molecules themselves predict poor prognosis in HGSOC and associate with an activated αSMA+/FAP+ fibroblast phenotype regulated by TGFβR activity and Hh signaling.

We used the knowledge gained from our previous analysis of HGSOC metastases, further studies on HGSOC biopsies, *in silico* analysis, and *in vitro* cultures to inform and build a relevant 3D multi-cellular model of the tumor microenvironment. We facilitated sustained production of key matrisome proteins in tri-cultures by cell types also found in patient biopsies, and RNAseq analysis demonstrated that several important features of the diseased biopsies, especially related to ECM regulation, cell adhesion, and migration, as well as the MI gene expression signature, were enhanced in the tri-cultures. Interestingly, compared to responses with monolayers on stiff plastic, FAP expression was significantly downregulated, and CTSB expression was also downregulated with the inhibitor combination in tri-cultures. These

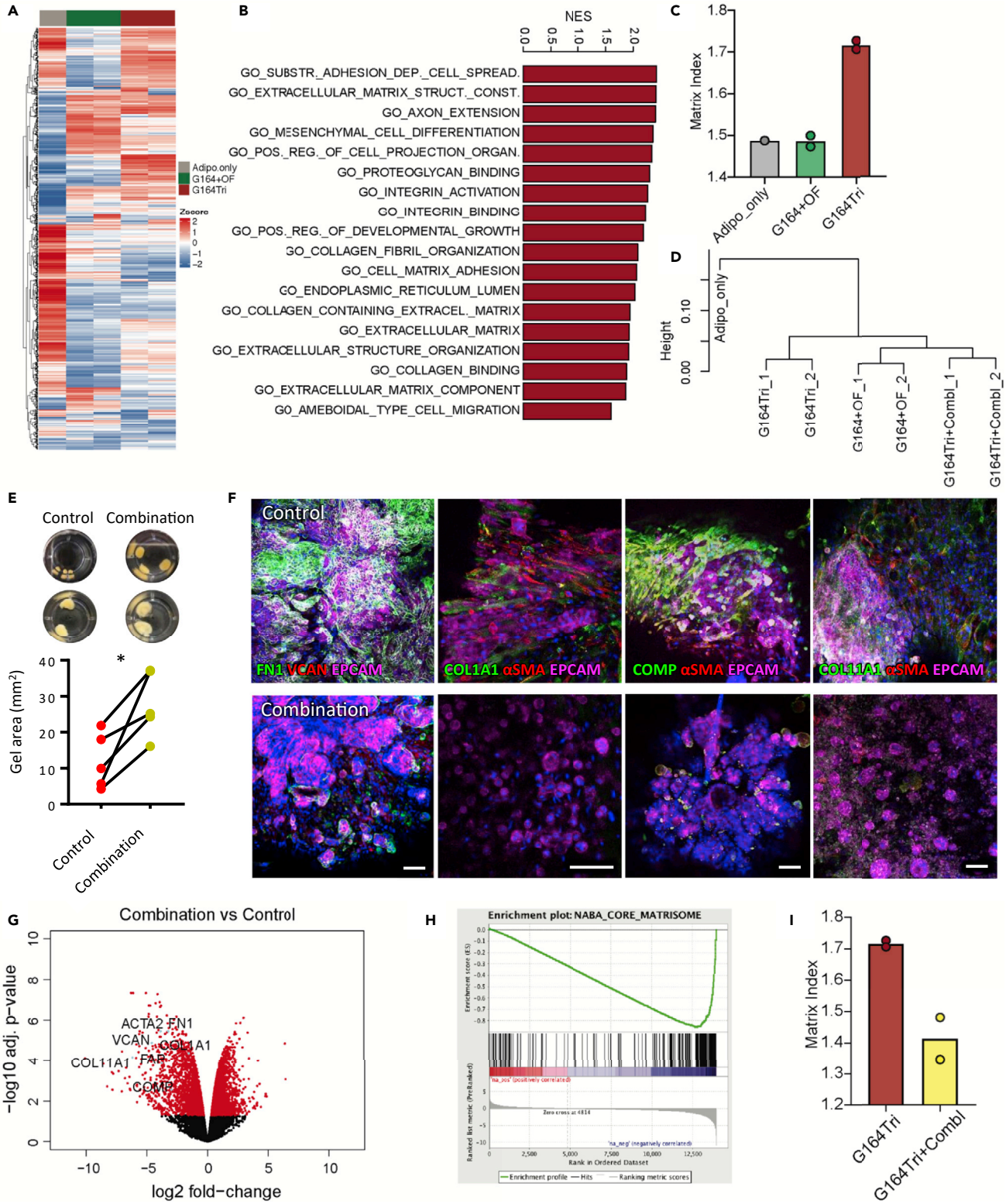

Figure 7. TGFβR and GLI1/2 inhibitor combination reduces tumor matrix expression in HGSOC tri-cultures

RNAseq was performed on adipocyte-only gels (Adipo_only), control tri-cultures (G164Tri), G164 + OF co-cultures, and G164Tri treated with inhibitor combination (G164Tri + CombI).

(A) Heatmap of all matrisome genes detected in Adipo_only, G164 + OF, and G164Tri.

Figure 7. *Continued*

(B) GSEA was performed on differentially expressed genes in G164Tri vs G164 + OF; bar plot indicates normalized enrichment scores (NES) for the indicated gene ontologies ($p < 0.05$).

(C) Matrix index was calculated from the RNAseq data across the samples.

(D) Hierarchical cluster analysis of transcriptomes for indicated samples.

(E) After 21 days of culture, gel areas of control and combination-treated tri-cultures were measured from images (insets show 2 different experiments); data are mean of 2–4 gels per experiment (N = 5), $p < 0.05$ (two-way, paired t test).

(F and G) (F) IF on tri-cultures for EPCAM, αSMA, FN1, VCAN, COL1A1, COMP, COL11A1, and DAPI (blue), scale bars represent 100 μm. G164Tri was treated with inhibitor combination and subjected to RNAseq (G) Volcano plot used to visualize changes in expression between G164Tri treated with inhibitors (G164Tri + CombI) and control G164Tri. Red dots indicate adjusted P value <0.05.

(H) GSEA performed on the differentially expressed genes between G164Tri + CombI and G164Tri; enrichment plot derived from GSEA of RNA sequencing data of G164 tri-cultures.

(I) Matrix index for G164Tri and G164Tri + CombI. For RNA sequencing, 2 gels were pooled per sample, Adipo_only (n = 1), G164Tri, and G164Tri + CombI (n = 2).Scale bars represent 100 μm.

differences implicate the importance of a physiologically relevant biomechanical environment, and our results show that human 3D multi-cellular models can be useful for studying some aspects of cancer biology.

We demonstrated that TGFβ signaling plays a powerful role in induction of an aggressive fibroblast phenotype, which is responsible for deposition of disease-associated matrix that predicts poor prognosis. TGFβ ligands play important roles in development, homeostasis, and wound healing, and all three known isoforms act through the same receptor signaling pathway (Kubiczkova et al., 2012). The TGFβ pathway is widely acknowledged as essential for tumor progression and can play pivotal roles as both a promoter and suppressor of cancer cells. Cancer cells can acquire loss-of-function mutations and lose responsiveness to TGFβ, thereby bypassing cell cycle arrest (Zhang et al., 2018). TGFβ plays an important role in recruitment and activation of cells of the innate immune system but also acts to suppress immune cell functions (Yang et al., 2010). Additionally, TGFβ plays an essential role in regulation of the adaptive immune system, and its continued presence can suppress T-cell functions and promote pro-tumorigenic phenotypes (Caja et al., 2018; Tauriello et al., 2018).

More recently, TGFβ has been recognized for its potential regulatory role in the stromal microenvironment, which in turn plays an important role in tumor progression. In our study, we identified that malignant cell lines expressed all three TGFβ isoforms, and TGFβ-2/3 ligands were upregulated compared to our non-malignant control with the greatest increase for TGFβ3. TGFβ3 has previously been associated with a set of poor outcome genes in serous ovarian cancer (Cheon et al., 2014). We showed that TGFβ3 induced αSMA, FAP, and GLI1 expression in OFs and promoted production of five upregulated MI molecules. Of particular interest is a recently published bioinformatics analysis of pan-cancer transcriptional ECM regulation in cancer (Chakravarthy et al., 2018). Chakravarthy *et al* reported that their ECM signature was linked to TGFβ signaling and was a biomarker of failure to respond to immune checkpoint blockade (Chakravarthy et al., 2018). Response to an anti-PDL1 agent in patients with metastatic bladder cancer was also associated with increased TGFβ signaling in patient biopsies (Mariathasan et al., 2018) and treatment of tumor-bearing mice with inhibitors of TGFβ or its receptor enhanced response to anti-PD1/PDL-1 therapies (Tauriello et al., 2018) (Mariathasan et al., 2018).

Further evidence for the role of TGFβ in HGSOC progression comes from related 3D culture experiments. We developed a tetra-culture, comprising layers of human adipocytes, fibroblasts, mesothelial cells, and malignant cells, to model the role of platelets in early HGSOC metastases to the omentum (Malacrida et al., 2021). TGFβ, particularly from platelets, was again implicated in ECM deposition but also malignant cell EMT and invasion via actions on both malignant cells and mesothelial cells.

In this paper, we have also highlighted apparent cross talk between TGFβR and Hh, as both pathways promote αSMA in OFs such that TGFβR stimulates GLI1 signaling leading to increased αSMA expression. FN1 and VCAN were upregulated by TGFβ, in agreement with previous studies, but Hh appeared to have little involvement. However, there was a strong indication that Hh enhances COL1A1, COL11A1, and COMP and that the GLI1/2 inhibitor created a synergistic inhibitory effect when used with the TGFβR inhibitor. Interestingly, the GLI1/2 inhibitor did not influence matrix molecule expression in malignant cells, even in AOCS1, which had enriched Hh-GLI pathway activity, implying that the signaling mechanisms either have a functional loss or are different between cell types. However, GLI1/2 inhibition did

reduce proliferation in AOCS1. In addition, expression of Hh ligands was not detected in either HGSOC cell line, indicating that GLI1 activation in OFs was not due to malignant cell-secreted Hh ligands. These two separate observations of inhibition synergy and GLI1 stimulation by TGFβ signaling suggest that Hh is likely to be activated by more than one pathway, and therefore, inhibition of TGFβR activity does not silence all Hh activity. This demonstrates potential for use of GLI inhibitors in cancers that have poor prognostic Hh-stromal signatures and malignant cell Hh activity, and there may be added benefit from combination treatment with TGFβR inhibitors. Currently, the most clinically advanced group of Hh inhibitors targets smoothened (SMO) inhibitors (Pak and Segal, 2016), which is upstream of GLI1. However, there have been cases where malignant cells developed clinical resistance to SMO inhibitors via a number of different mechanisms (Pak and Segal, 2016) and therefore directly targeting GLI may offer more promise in bypassing SMO-resistant cells.

All six upregulated MI molecules have previously been linked to tumor progression. In particular, COL11A1 expression is consistently linked with poor prognosis in solid metastatic carcinomas (Cheon et al., 2014; Vazquez-Villa et al., 2015; Jia et al., 2016). While COL11A1 has been implicated as a specific biomarker of activated fibroblasts (Jia et al., 2016), it can also be expressed in epithelial cells with high metastatic potential (Vazquez-Villa et al., 2015). Indeed, in this study, we demonstrated that AOCS1 was highly positive for COL11A1, and there was malignant cell nuclear positivity in >50% of our biopsies. Interestingly, in our cells, COL11A1 was intracellular and highly expressed in cells with active Hh signaling. Use of the inhibitor combination on OFs caused a total breakdown of COL11A1 fibrous structure, in line with loss of αSMA stress fibers, suggesting a role in forming a stable and contractile phenotype. We believe that this warrants further investigation.

In conclusion, the main drive for creating human models of the tumor microenvironment is to study processes governing disease progression in a more physiologically relevant setting and to aid pre-clinical testing. The multi-cellular model we describe here could be useful for screening compounds that could modify the malignant matrisome that associates with poor prognosis in 13 common human cancers. The most promising candidates could then be tested in mouse models that most closely replicate the human TME, either patient-derived xenografts or models such as our recently published new syngeneic mouse HGSOC models that replicate many features of the human omental TME (Maniati et al., 2020).

In our model, TGFβR and GLI inhibitors attenuated fibroblast activation and tumor-associated matrix production while preventing malignant cells from forming large spheroid growths. Therefore, inhibitors of these pathways may have clinical potential, alone or in combination. While we do not know if these processes have the potential to increase malignant cell dissemination due to removal of the physical matrix barrier, it is also possible that this may facilitate better access for cancer treatments or immune cells. We believe that our novel tri-culture model will be a useful first step in pre-clinical evaluation of therapies targeting a dysregulated matrix in human solid cancers and their effect on immune cell access to malignant cells. Moreover, we believe that our work demonstrates the usefulness of using a combination of mono-, co-, and multi-cellular cultures to understand cell-cell interactions in the tumor microenvironment.

Limitations of the study

While we were able to validate data obtained from analyses of human tumor biopsies in the tri-culture model, there may be other cells and signaling pathways involved in the regulation of poor prognostic ECM molecules in a more complex tumor microenvironment. In future studies, we aim to increase the complexity of the models. We have already shown that it is feasible and valuable to include mesothelial cells in our multi-cellular models (Malacrida et al., 2021) and are currently adding myeloid cells to investigate further signaling pathways that regulate poor prognostic ECM molecules.

STAR★METHODS

Detailed methods are provided in the online version of this paper and include the following:

- KEY RESOURCES TABLE
- RESOURCE AVAILABILITY
  - Lead Contact
  - Materials availability
  - Data and code availability

SUPPLEMENTAL INFORMATION

Supplemental information can be found online at https://doi.org/10.1016/j.isci.2021.102674.

ACKNOWLEDGMENTS

The authors wish to acknowledge the role of the Barts Cancer Institute Tissue Bank Team in collecting and making available the samples used for this publication. We thank Barts Trust Oncology Surgeons for sample provision. We also thank Dr Chiara Berlato, Anissa Lakhani, Joash Joy, and Priyanka Hirani for technical help and George Elia and the BCI Pathology Core, Professor David Bowtell, and Professor Ronny Drapkin for kindly providing cell lines. Finally, we express our gratitude to the patients for donating the samples without which this work would not have been possible. This project was funded by the European Research Council (ERC322566) and Cancer Research UK (A16354, A13034, A19694 and A25714). L.S.M.L. was funded by a grant from the Institute of Bioengineering, Queen Mary University of London.

AUTHOR CONTRIBUTIONS

R.M.D.-S. designed research studies, conducted experiments, acquired data, analyzed data, and wrote the paper. S.N. conducted experiments and acquired data. E.M. analyzed data and wrote the paper. B.M. conducted experiments and acquired data. R.R. conducted experiments and acquired data. R.R.J. conducted experiments and acquired data. L.S.M.L. conducted experiments and acquired data. O.M.T.P. designed research studies and wrote the paper. M.K. designed research studies and wrote the paper. F.R.B. designed research studies and wrote the paper.

DECLARATION OF INTERESTS

F.R.B. is a Scientific Advisory Board Member for Verseau Therapeutics Inc. and has received honoraria from GlaxoSmithKline and Novartis.

INCLUSION AND DIVERSITY

We worked to ensure diversity in experimental samples through the selection of the cell lines. One or more of the authors of this paper self-identifies as an underrepresented ethnic minority in science. The author list of this paper includes contributors from the location where the research was conducted who participated in the data collection, design, analysis, and/or interpretation of the work.

All authors agree to inclusion of this statement.

Received: February 2, 2021
Revised: April 1, 2021
Accepted: May 27, 2021
Published: June 25, 2021

REFERENCES

Anders, S., Pyl, P.T., and Huber, W. (2014). HTSeq—a Python framework to work with high-throughput sequencing data. Bioinformatics *31*, 166–169.

Avgustinova, A., Iravani, M., Robertson, D., Fearns, A., Gao, Q., Klingbeil, P., Hanby, A.M., Speirs, V., Sahai, E., Calvo, F., and Isacke, C.M. (2016). Tumour cell-derived Wnt7a recruits and activates fibroblasts to promote tumour aggressiveness. Nat Commun. *7*, 10305.

Bhowmick, N.A., Neilson, E.G., and Moses, H.L. (2004). Stromal fibroblasts in cancer initiation and progression. Nature *432*, 332–337.

Caja, L., Dituri, F., Mancarella, S., Caballero-Diaz, D., Moustakas, A., Giannelli, G., and Fabregat, I. (2018). TGF-beta and the tissue microenvironment: relevance in fibrosis and cancer. Int J Mol Sci. *19*.

Calvo, F., Ege, N., Grande-Garcia, A., Hooper, S., Jenkins, R.P., Chaudhry, S.I., Harrington, K., Williamson, P., Moeendarbary, E., Charras, G., and Sahai, E. (2013). Mechanotransduction and YAP-dependent matrix remodelling is required for the generation and maintenance of cancer-associated fibroblasts. Nat. Cell Biol. *15*, 637–646.

Chakravarthy, A., Khan, L., Bensler, N.P., Bose, P., and De Carvalho, D.D. (2018). TGF-beta-associated extracellular matrix genes link cancer-associated fibroblasts to immune evasion and immunotherapy failure. Nat. Commun. *9*, 4692.

Cheon, D.J., Tong, Y., Sim, M.S., Dering, J., Berel, D., Cui, X., Lester, J., Beach, J.A., Tighiouart, M., Walts, A.E., et al. (2014). A collagen-remodeling gene signature regulated by TGF-beta signaling is associated with metastasis and poor survival in serous ovarian cancer. Clin. Cancer Res. *20*, 711–723.

Desmouliere, A., Chaponnier, C., and Gabbiani, G. (2005). Tissue repair, contraction, and the myofibroblast. Wound Repair Regen. *13*, 7–12.

Didiasova, M., Singh, R., Wilhelm, J., Kwapiszewska, G., Wujak, L., Zakrzewicz, D., Schaefer, L., Markart, P., Seeger, W., Lauth, M., and Wygrecka, M. (2017). Pirfenidone exerts antifibrotic effects through inhibition of GLI transcription factors. FASEB J. *31*, 1916–1928.

Englund, E., Bartoschek, M., Reitsma, B., Jacobsson, L., Escudero-Esparza, A., Orimo, A., Leandersson, K., Hagerling, C., Aspberg, A., Storm, P., et al. (2016). Cartilage oligomeric matrix protein contributes to the development and metastasis of breast cancer. Oncogene, 5585–5596.

Erdogan, B., Ao, M., White, L.M., Means, A.L., Brewer, B.M., Yang, L., Washington, M.K., Shi, C., Franco, O.E., Weaver, A.M., et al. (2017). Cancer-associated fibroblasts promote directional cancer cell migration by aligning fibronectin. J. Cell Biol. *216*, 3799–3816.

Farkas, I.J., Szanto-Varnagy, A., and Korcsmaros, T. (2012). Linking proteins to signaling pathways for experiment design and evaluation. PLoS One *7*, e36202.

Hanley, C.J., Noble, F., Ward, M., Bullock, M., Drifka, C., Mellone, M., Manousopoulou, A., Johnston, H.E., Hayden, A., Thirdborough, S., et al. (2016). A subset of myofibroblastic cancer-associated fibroblasts regulate collagen fiber elongation, which is prognostic in multiple cancers. Oncotarget *7*, 6159–6174.

Horn, A., Palumbo, K., Cordazzo, C., Dees, C., Akhmetshina, A., Tomcik, M., Zerr, P., Avouac, J., Gusinde, J., Zwerina, J., et al. (2012). Hedgehog signaling controls fibroblast activation and tissue fibrosis in systemic sclerosis. Arthritis Rheum. *64*, 2724–2733.

Javelaud, D., Pierrat, M.J., and Mauviel, A. (2012). Crosstalk between TGF-beta and hedgehog signaling in cancer. FEBS Lett. *586*, 2016–2025.

Jia, D., Liu, Z., Deng, N., Tan, T.Z., Huang, R.Y., Taylor-Harding, B., Cheon, D.J., Lawrenson, K., Wiedemeyer, W.R., Walts, A.E., et al. (2016). A COL11A1-correlated pan-cancer gene signature of activated fibroblasts for the prioritization of therapeutic targets. Cancer Lett. *382*, 203–214.

Kenny, H.A., Chiang, C.Y., White, E.A., Schryver, E.M., Habis, M., Romero, I.L., Ladanyi, A., Penicka, C.V., George, J., Matlin, K., et al. (2014). Mesothelial cells promote early ovarian cancer metastasis through fibronectin secretion. J. Clin. Invest. *124*, 4614–4628.

Klingberg, F., Hinz, B., and White, E.S. (2013). The myofibroblast matrix: implications for tissue repair and fibrosis. J. Pathol. *229*, 298–309.

Kubiczkova, L., Sedlarikova, L., Hajek, R., and Sevcikova, S. (2012). TGF-beta - an excellent servant but a bad master. J. Transl Med. *10*, 183.

Laklai, H., Miroshnikova, Y.A., Pickup, M.W., Collisson, E.A., Kim, G.E., Barrett, A.S., Hill, R.C., Lakins, J.N., Schlaepfer, D.D., Mouw, J.K., et al. (2016). Genotype tunes pancreatic ductal adenocarcinoma tissue tension to induce matricellular fibrosis and tumor progression. Nat. Med. 497–505.

Love, M.I., Huber, W., and Anders, S. (2014). Moderated estimation of fold change and dispersion for RNA-seq data with DESeq2. Genome Biol. *15*, 550.

Malacrida, B., Nichols, S., Maniati, E., Jones, R., Delaine-Smith, R., Roozitalab, R., Tyler, E., Thomas, M., Boot, G., Mackerodt, J., et al. (2021). A human multi-cellular model shows how platelets drive production of diseased extracellular matrix and tissue invasion. iScience.

Maniati, E., Berlato, C., Gopinathan, G., Heath, O., Kotantaki, P., Lakhani, A., Mcdermott, J., Pegrum, C., Delaine-Smith, R.M., Pearce, O.M.T., et al. (2020). Mouse ovarian cancer models recapitulate the human tumor microenvironment and patient response to treatment. Cell Rep. *30*, 525–540 e7.

Mariathasan, S., Turley, S.J., Nickles, D., Castiglioni, A., Yuen, K., Wang, Y., Kadel, E.E., III, Koeppen, H., Astarita, J.L., Cubas, R., et al. (2018). TGFbeta attenuates tumour response to PD-L1 blockade by contributing to exclusion of T cells. Nature *554*, 544–548.

Mihaly, Z., Kormos, M., Lanczky, A., Dank, M., Budczies, J., Szasz, M.A., and Gyorffy, B. (2013). A meta-analysis of gene expression-based biomarkers predicting outcome after tamoxifen treatment in breast cancer. Breast Cancer Res. Treat. *140*, 219–232.

Milagre, C.S., Gopinathan, G., Everitt, G., Thompson, R.G., Kulbe, H., Zhong, H., Hollingsworth, R.E., Grose, R., Bowtell, D.D., Hochhauser, D., and Balkwill, F.R. (2015). Adaptive upregulation of EGFR limits attenuation of tumor growth by neutralizing IL6 antibodies, with implications for combined therapy in ovarian cancer. Cancer Res. *75*, 1255–1264.

Mootha, V.K., Lindgren, C.,M., Eriksson, C.M., Subramanian, A., Sihag, S., Lehar, J., Puigserver, P., Carlsson, E., and Ridderstrale, M.E.A. (2003). PGC-1 alpha-responsive genes involved in oxidative phosphorylation are coordinately downregulated in human diabetes. Nat. Genet. *34*, 267–273.

Nieman, K.M., Kenny, H.A., Penicka, C.V., Ladanyi, A., Buell-Gutbrod, R., Zillhardt, M.R., Romero, I.L., Carey, M.S., Mills, G.B., Hotamisligil, G.S., et al. (2011). Adipocytes promote ovarian cancer metastasis and provide energy for rapid tumor growth. Nat. Med. *17*, 1498–1503.

Pak, E., and Segal, R.A. (2016). Hedgehog signal transduction: key players, oncogenic drivers, and cancer therapy. Dev. Cell *38*, 333–344.

Patch, A.M., Christie, E.L., Etemadmoghadam, D., Garsed, D.W., George, J., Fereday, S., Nones, K., Cowin, P., Alsop, K., Bailey, P.J., et al. (2015). Whole-genome characterization of chemoresistant ovarian cancer. Nature *521*, 489–494.

Pearce, O.M.T., Delaine-Smith, R.M., Maniati, E., Nichols, S., Wang, J., Bohm, S., Rajeeve, V., Ullah, D., Chakravarty, P., Jones, R.R., et al. (2018). Deconstruction of a metastatic tumor microenvironment reveals a common matrix response in human cancers. Cancer Discov. *8*, 304–319.

Ritchie, M.E., Phipson, B., Wu, D., Hu, Y., Law, C.W., Shi, W., and Smyth, G.K. (2015). Limma powers differential expression analyses for RNA-sequencing and microarray studies. Nucleic Acids Res. *43*, e47.

Robinson, M.D., and Oshlack, A. (2010). A scaling normalization method for differential expression analysis of RNA-seq data. Genome Biol. *11*, R25.

Ruan, H., Hao, S., Young, P., and Zhang, H. (2015). Targeting cathepsin B for cancer therapies. Horiz. Cancer Res. *56*, 23–40.

Sahai, E., Astsaturov, I., Cukierman, E., Denardo, D.G., Egeblad, M., Evans, R.M., Fearon, D., Greten, F.R., Hingorani, S.R., Hunter, T., et al. (2020). A framework for advancing our understanding of cancer-associated fibroblasts. Nat. Rev. Cancer *20*, 174–186.

Schneider, R.K., Mullally, A., Dugourd, A., Peisker, F., Hoogenboezem, R., Van Strien, P.M.H., Bindels, E.M., Heckl, D., Busche, G., et al. (2018). Gli1(+) mesenchymal stromal cells are a key driver of bone marrow fibrosis and an important cellular therapeutic target. Cell Stem Cell *23*, 308–309.

Shiga, K., Hara, M., Nagasaki, T., Sato, T., Takahashi, H., and Takeyama, H. (2015). Cancer-associated fibroblasts: their characteristics and their roles in tumor growth. Cancers (Basel) *7*, 2443–2458.

Subramanian, A., Tamayo, P., Mootha, V.K., Mukherjee, S., Ebert, B.L., Gillette, M.A., Paulovich, A., Pomeroy, S.L., Golub, T.R., Lander, E.S., and Mesirov, J.P. (2005). Gene set enrichment analysis: a knowledge-based approach for interpreting genome-wide expression profiles *102*, 15545–15550.

Tamura, N., Shaikh, N., Muliaditan, D., Soliman, T.N., Mcguinness, J.R., Maniati, E., Moralli, D., Durin, M.A., Green, C.M., Balkwill, F.R., et al. (2020). Specific mechanisms of chromosomal instability indicate therapeutic sensitivities in high-grade serous ovarian carcinoma. Cancer Res. *80*, 4946–4959.

Tauriello, D.V.F., Palomo-Ponce, S., Stork, D., Berenguer-Llergo, A., Badia-Ramentol, J., Iglesias, M., Sevillano, M., Ibiza, S., Canellas, A., Hernando-Momblona, X., et al. (2018). TGFbeta drives immune evasion in genetically reconstituted colon cancer metastasis. Nature *554*, 538–543.

Thompson, C.L., Patel, R., Kelly, T.A., Wann, A.K., Hung, C.T., Chapple, J.P., and Knight, M.M. (2015). Hedgehog signalling does not stimulate cartilage catabolism and is inhibited by Interleukin-1beta. Arthritis Res. Ther. *17*, 373.

Tian, H., Callahan, C.A., Dupree, K.J., Darbonne, W.C., Ahn, C.P., Scales, S.J., and De Sauvage, F.J. (2009). Hedgehog signaling is restricted to the stromal compartment during pancreatic carcinogenesis. Proc. Natl. Acad. Sci. U S A *106*, 4254–4259.

Tothill, R.W., Tinker, A.V., George, J., Brown, R., Fox, S.B., Lade, S., Johnson, D.S., Trivett, M.K., Etemadmoghadam, D., Locandro, B., et al. (2008). Novel molecular subtypes of serous and endometroid ovarian cancer linked to clinical outcome. Clin. Cancer Res. *14*, 5198–5208.

Vazquez-Villa, F., Garcia-Ocana, M., Galvan, J.A., Garcia-Martinez, J., Garcia-Pravia, C., Menendez-Rodriguez, P., Gonzalez-Del Rey, C., Barneo-Serra, L., and De Los Toyos, J.R. (2015). COL11A1/(pro)collagen 11A1 expression is a remarkable biomarker of human invasive carcinoma-associated stromal cells and carcinoma progression. Tumour Biol. *36*, 2213–2222.

Waalkes, S., Atschekzei, F., Kramer, M.W., Hennenlotter, J., Vetter, G., Becker, J.U., Stenzl, A., Merseburger, A.S., Schrader, A.J., Kuczyk, M.A., and Serth, J. (2010). Fibronectin 1 mRNA expression correlates with advanced disease in renal cancer. BMC Cancer *10*, 503.

Wang, B., Fallon, J.F., and Beachy, P.A. (2000). Hedgehog-regulated processing of Gli3 produces an anterior/posterior repressor gradient in the developing vertebrate limb. Cell *100*, 423–434.

Yang, L., Pang, Y., and Moses, H.L. (2010). TGF-beta and immune cells: an important regulatory axis in the tumor microenvironment and progression. Trends Immunol. *31*, 220–227.

Yeung, T.L., Leung, C.S., Wong, K.K., Samimi, G., Thompson, M.S., Liu, J., Zaid, T.M., Ghosh, S., Birrer, M.J., and Mok, S.C. (2013). TGF-beta modulates ovarian cancer invasion by upregulating CAF-derived versican in the tumor microenvironment. Cancer Res. *73*, 5016–5028.

Yeung, T.L., Sheng, J., Leung, C.S., Li, F., Kim, J., Ho, S.Y., Matzuk, M.M., Lu, K.H., Wong, S.T.C., and Mok, S.C. (2018). Systematic identification of druggable epithelial-stromal crosstalk signaling networks in ovarian cancer. J. Natl. Cancer Inst. 272–282.

Zhang, Q., Hou, X., Evans, B.J., Vanblaricom, J.L., Weroha, S.J., and Cliby, W.A. (2018). LY2157299 monohydrate, a TGF-betaR1 inhibitor, suppresses tumor growth and ascites development in ovarian cancer. Cancers (Basel) *10*, 260.

STAR★METHODS

KEY RESOURCES TABLE

REAGENT or RESOURCE	SOURCE	IDENTIFIER
Antibodies		
Monoclonal Mouse Anti Alpha Smooth Muscle Actin	Sigma	Cat# A2547; RRID:AB_476701
Monoclonal Mouse Anti Actin	Sigma	Cat# A1978; RRID:AB_476692
Polyclonal Rabbit Anti Versican	Sigma	Cat# HPA004726; RRID:AB_1080561
Polyclonal Rabbit Anti COL11A1	Sigma	Cat# HPA052246; RRID: N/A
Polyclonal Rabbit Anti COL1A1	Sigma	Cat# HPA011795; RRID:AB_1847088
Polyclonal Rabbit Anti FN1	Sigma	Cat# F3648; RRID:AB_476976
Monoclonal Mouse Anti Ki67	Dako	Cat# M7240; RRID:AB_2142367
Monoclonal Rabbit anti-fibroblast activation protein, alpha	Abcam	Cat# ab207178; RRID:AB_2864720
Monoclonal Rat anti COMP	Abcam	Cat# ab11056; RRID:AB_297708
Monoclona Mouse anti CTSB	Abcam	Cat# ab58802; RRID:AB_940824
Polyclonal Rabbit anti PAX8	Novus	Cat# NBP1-32440; RRID:AB_2283498
Human anti EpCAM Alexa Flour 488	Thermo Fisher	Cat# 53-8326-41; RRID:AB_11220074
Monoclonal Mouse anti GLI1	Santa Cruz Biotechnology	Cat# sc-515751; RRID: N/A
Human Fibroblast Activation Protein alpha PE-conjugated Antibody (FAP-PE) (Clone # 427819)	R&D systems	Cat# FAB3715P; RRID: N/A
Human alpha-Smooth Muscle Actin APC-conjugated Antibody (αSMA-APC) (Clone #1A4)	R&D systems	Cat# IC1420A; RRID:AB_10890600
Alexa Fluor 568 Phalloidin	ThermoFisher	Cat# A12380; RRID: N/A
Biotinylated goat anti-rabbit IgG antibody 1.5mg	Vector Labs	Cat# BA-1000; RRID:AB_2313606
Biotinylated goat anti-rabbit IgG antibody 1.5mg	Vector Labs	Cat# BA-9200; RRID:AB_2336171
Anti-TGF beta 1 antibody [2Ar2]	Abcam	Cat# ab64715; RRID:AB_1144265
Biological samples		
Formalin Fixed Paraffin Embedded Human Omental Blocks	Barts Cancer Institute - Gynae-oncology Biobank	(https://directory.biobankinguk.org/Profile/Biobank/GBR-1-128) HTA license number 12199 (REC no: 10/H0304/14 and 15/EE/0151)
Chemicals, peptides, and recombinant proteins		
Trypsin-EDTA solution 10X	Sigma	T4174
DMEM/F12 with Glutamax	Thermo Fisher Scientific	31331093
FBS	Fisher Scientific	10500-064
Collagenase type I powder	Thermo Fisher Scientific	17100017
Cholera Toxin from *Vibrio cholerae*	Sigma	C8052-.5MG
Recombinant Human TGFb3	Peprotech	100-36E
SB431542 hydrate	Sigma	S4317
Hh/Gli Antagonist, GANT61 - CAS 500579-04-4 - Calbiochem	Merck	373403
L-Ascorbic acid 2-phosphate sesquimagnesium salt hydrate	Sigma	A8960

(*Continued on next page*)

Continued

REAGENT or RESOURCE	SOURCE	IDENTIFIER
Collagen I from rat tail	Thermo Fisher Scientific	A1048301
DMEM low glucose 10x	Sigma	D2429
Permeabilization Buffer (10X)	eBioscience	00-8333-56
Fixation/Permeabilization Diluent	eBioscience	00-5223-56
Fixation/Permeabilization Concentrate	eBioscience	00-5123-43
Goat serum 100ml	Life Technologies	16210064
Fixable Viability Dye eFluor 450	eBioscience	65-0863-18
Agilent RNA 6000 Pico Reagents	Agilent	5067-1514
Medium-199	Thermo Fisher Scientific	22350029
Fluorescein diacetate	Sigma	F7378-5G
Ethidium Homodimer I Solution	Sigma	E1903
Insulin-Transferrin-Selenium-Sodium Pyruvate (ITS-A) (100X)	Thermo Fisher Scientific	51300044
Zytomed Antibody diluent	Bioscience LifeSciences	ZUC025-500
Bovine Serum Albumin	Sigma	A4503
Hydrogen Peroxide 30% (w/v) (100 Volumes), Extra Pure SLR, Fisher Chemical	Fisher Scientific	10687022
Vectastain Elite ABC HRP Kit	Vector Laboratories	PK-6100
SIGMAFAST DAB Tablets	Sigma	D4293
Hematoxylin Solution, Gill No. 1	Sigma	GHS116
Formalin solution neutral buffered 10%	Sigma	HT501128-4L
DPX Mountant for histology	Sigma	06522
Triton X-100	Sigma	T8787
DAPI	Biotium	40043
Critical commercial assays		
RNeasy Micro Kit (50)	Qiagen	74004
TGFb3 ELISA kit	Abcam	272203
High-Capacity cDNA Reverse Transcription Kit (200 reactions)	Thermo Fisher Scientific	4368814
iTaq™ Universal Probes Supermix (10 x 1ml)	Biorad	1725132
Deposited data		
RNASeq on HGSOC cell-line mono-cultures and tri-cultures	GEO	GSE125109
Experimental models: Cell lines		
Human AOCS1	Kindly gifted by Prof D Bowtell's lab	Tamura et al., 2020. https://doi.org/10.1158/0008-5472.CAN-19-0852. Epub 2020 Sep 30. PMID: 32998996.
Human G164	isolated in our lab	Tamura et al., 2020. https://doi.org/10.1158/0008-5472.CAN-19-0852. Epub 2020 Sep 30. PMID: 32998996.
Oligonucleotides		
	See Table S5	N/A
Software and algorithms		
FlowJo 9.4.6	Treestar Inc.	https://www.flowjo.com/
GraphPad Prism 8.3.0	GraphPad	https://www.graphpad.com/scientific-software/prism/

(*Continued on next page*)

Continued

REAGENT or RESOURCE	SOURCE	IDENTIFIER
R 3.1.3	NA	http://www.R-project.org
Definiens	Definiens Inc.	N/A
HTSeq	https://htseq.readthedocs.io/en/release_0.11.1/	Anders et al., 2014
EdgeR	Bioconductor	Robinson and Oshlack, 2010
Limma	Bioconductor	Ritchie et al., 2015
GSEA	https://www.genepattern.org/	Subramanian et al., 2005
Biorender	https://biorender.com/	Some graphical abstract components were created with Biorender.com

RESOURCE AVAILABILITY

Lead Contact

Further information and requests for resources and data should be directed to the lead contact, Frances Balkwill (f.balkwill@qmul.ac.uk), Barts Cancer Institute, Queen Mary University of London Charterhouse Square EC1M 6BQ, London, UK.

Materials availability

This study did not generate new unique reagents.

Data and code availability

The accession number for the RNASeq data reported in this paper is Gene Expression Omnibus (GEO): GSE125109.

EXPERIMENTAL MODELS AND SUBJECT DETAILS

Ovarian cancer patient samples and study approval

Patient samples were kindly donated by women with HGSOC undergoing surgery at Barts Health NHS Trust. Tissue deemed by a pathologist to be surplus to diagnostic and therapeutic requirement were collected together with associated clinical data under the terms of the Barts Gynae Tissue Bank (HTA license number 12199. REC no: 10/H0304/14). The patients ages ranged from 40-87. Each patient gave written informed consent and all tissue used for this study was approved by a UK national review board. Studies were conducted in accordance with the Declaration of Helsinki and International Ethical Guidelines for Biomedical Research Involving Human Subjects (CIOMS).

HGSOC cell lines

The AOCS1 cell line was established in our laboratory from an omental HGSOC tumor collected during interval debulking surgery in 2011 (Milagre et al., 2015). The G164 cell line was established in our laboratory from an omental HGSOC tumor collected during interval debulking surgery in 2015. G164 cells were TP53 and PAX8 positive (Tamura et al., 2020). Malignant cells were cultured in DMEM:F12 (Gibco), 10% FCS, 1% penicillin and streptomycin in a 5% CO2 humidified incubator at 37°C. The immortalized human FTSE cell line, wild-type FT318, was kindly given by Professor Ronny Drapkin (Perelman School of Medicine, University of Pennsylvania) and grown in serum-free WIT-P medium (Cellaria) without antibiotics and 100ng/ml cholera toxin (Sigma-Aldrich). Quality control of all cell lines was carried out by frequent STR analysis (Eurofins MWG), mycoplasma testing (InvivoGen) and cell lines were used for 4 to 5 passages.

METHOD DETAILS

RNA *in situ* hybridization

Sections (4 μm) of formalin-fixed paraffin embedded (FFPE) human omentum samples were deparaffinised, treated with hydrogen peroxide and boiled in the target retrieval reagent. Sections were dried in ethanol and left at room temperature (RT) overnight. Slides were incubated in protease reagent at 40°C in a HyBEZ Hybridization System (Advanced Cell Diagnostics Inc. USA) followed by incubation at 40°C with the gene-specific probe. The AMP 1-6 reagents were all subsequently hybridized as specified in the manufacturer's

instructions. Labeled mRNAs were visualized using DAB reagent and counterstained using 50% Gill's hematoxylin. Counterstained slides were dehydrated using 70% and 95% ethanol and cleared in xylene before mounting coverslips using DPX. RNAscope® probes: FN1 (Hs-FN1 310311), COL1A1 (Hs-COL1A1 401891), VCAN (Hs-VCAN 430071), CTSB (Hs-CTSB 490251), COMP (Hs-COMP 457081), COL11A1 (Hs-COL11A1 400741), all from Advanced Cell Diagnostics.

Isolation of primary cells from human omentum

Fresh tissue was washed in phosphate buffered saline (PBS) and approximately 10cm^3 of omentum was submerged in 0.25% trypsin (Sigma-Aldrich) and incubated at 37°C for 20min to strip off any mesothelial cells. Trypsin was neutralized using DMEM:F12 1:1 medium (Gibco) with 10% heat-inactivated fetal bovine serum (FBS) (Hyclone). Tissue was washed with PBS, minced with dissection scissors into approximately 1-2mm pieces, suspended in DMEM (Sigma) with 5% FBS and 0.5 mg/ml collagenase type I (Gibco) and placed in a shaking incubator at 50rpm and 37°C for 75 min. Tissue digest was passed through 250 μM tissue strainers (Thermo-Fisher) and the floating adipocyte layer was carefully collected by pipette and washed by centrifuging twice for 5min at 200*g* in DMEM with 5% FBS. Adipocytes were used immediately for experiments. The stromal vascular fraction (SVF) pellet from the first wash was resuspended in DMEM:F12 1:1 + 10% FBS (growth medium) and cultured at 37°C, 5% CO_2. After three days, any unattached cells were washed away and attached cells were checked for fibroblastic morphology, and henceforth referred to as omental fibroblasts (OFs). Media was changed every 2-3 days and cells were passaged upon reaching confluence and used for experiments between passages 2-4. Multiple fibroblast donors were used for each experiment and data was plotted for each individual donor with no pooling. In total, fibroblasts from 23 different donors including from tissue with little disease and tissues with confirmed disease.

Monocultures

For mRNA extraction and flow cytometry, OFs were seeded at 200k and malignant cells were seeded at 500k in T25 flasks and grown for 4 days. For IF, OFs were seeded at 30k and malignant cells at 60k in 12-wells and grown for 4 days for cell markers and 14 days for matrix molecules. The appropriate factors and inhibitors were added 24h after seeding and replenished every 48h; recombinant TGFβ3 10ng/ml (Peprotech); SB431542 hydrate 20μM (Sigma-Aldrich); GANT61 7.5μM (InSolution, Merck); L-ascorbic acid-2-phopsphate (AA_2P) 50μg/ml (Sigma-Aldrich). AA2P was only added for experiments involving matrix production.

Collagen gel cultures

Collagen-gel solution (0.1w%) was made for 3D mono- and co-cultures mixing (per 100μl gel) 34μl of 3mg/ml rat-tail collagen I (Gibco), 4μl of 10x DMEM low-glucose (Sigma), 2μl of 1M NaOH and 60μl DMEM:F12 containing cells, prepared on ice. OF-only gels were seeded at 40k and grown for 7 days. Malignant cell-only gels were seeded at 80k and grown for 14 days. Co-cultures were seeded at a ratio of 1:1 (100k:100k) OFs to malignant cells and grown for 7 days. All gels were aliquoted at 100μl in 96-wells and incubated at 37°C, 5% CO_2 for 45min to set and then transferred to free-float in 24-wells with growth medium.

Flow-cytometry

For mono-layers, fibroblasts were detached using 0.5% trypsin-EDTA, centrifuged, washed in PBS and re-suspended in FACS buffer containing Human Fibroblast Activation Protein alpha PE-conjugated Antibody (FAP-PE) (R&D systems FAB3715P, Clone # 427819) on ice in darkness for 30 min. After centrifugation and washing in FACS buffer, cells were suspended in fixation/permeabilization solution (BD Biosciences) for 30 min on ice, washed in permeabilization/wash (PW) buffer, then incubated in 2% goat serum. Human alpha-Smooth Muscle Actin APC-conjugated Antibody (αSMA-APC) (R&D systems IC1420A, Clone #1A4) was added for 30 min before cells were washed in PW-buffer.

For gels containing cells, cultures were digested in 1mg/ml collagenase type I (Thermo-Fisher) in serum-free DMEM for 1hr with shaking at 110 rpm and 37°C. Gels were disaggregated with pipetting and 0.5% trypsin-EDTA (Sigma-Aldrich) was added at 37°C for 30 min. DMEM with 10% FBS was added 1:1 to the cell suspension and centrifuged at 200*g* for 5min. For live-dead assay, cells were resuspended in FACS buffer (PBS with 2mM EDTA, 2.5% BSA) containing Fixable Viability Dye eFluor 450 (FVD-e450) (eBioscience 65-0863-18) for 30 min on ice protected from light. After washes in FACS buffer, cells were fixed in neutral

buffered formalin. Stained samples were analyzed using an LSRFortessa cell analyzer (BD Biosciences) and data were analyzed with FlowJo 9.4.6 (Treestar Inc.).

Mechanical characterization of gels

Compression was performed using an Instron ElectroPulse E1000 (Instron, UK) equipped with a 10N load cell (resolution = 0.1 mN). Gels were submerged in PBS throughout testing. Gels were compressed using a stainless steel plane-ended platen with diameter > 2x gel diameter connected directly to the load cell. Gel thickness was measured as the distance between the base of the test dish and top of the gel, each detected by applying a pre-load of 0.3-5 mN. Tests were performed in displacement control mode and gels were displaced to 30% thickness at a rate of $1\%s^{-1}$ with the resulting load recorded. Gel modulus, a measure of material stiffness independent of specimen geometry, was calculated by converting load-data to stress (kPa) (load ÷ gel area), plotting a stress-strain curve and then taking the slope of the curve between 15-20% strain.

RNA isolation and real-time quantitative PCR

Total RNA was extracted using Qiagen RNeasy Plus Micro kit according to the manufacturer's instructions. Monolayers were first scrapped in RLT Plus buffer (Qiagen) and RNA was quantified using a NanoDrop 2000c (Thermo-Fisher Scientific). Tri-cultures were placed directly into RLT buffer and rigorously vortexed. RNA quality was analyzed on Agilent bioanalyzer 2100 using RNA PicoChips according to manufacturer's instructions. RNA integrity numbers were between 8.1 and 9.9. Total and reverse-transcription was carried out on 1μg of RNA using a T100 Thermal Cycler (Bio-Rad) and a High-Capacity cDNA Reverse Transcription Kit (Applied Biosystems) according to manufacturer's instructions. The PCR reaction was run on a StepOnePlus Real-Time PCR System (Applied Biosystems) using iTag Universal Probes Supermix (Applied Biosystems), FAM-MGB labeled Taqman gene expression probes and 5ng sample cDNA. Taqman gene expression assay targets; ACTA2 (Hs00426835_g1), FAP (Hs00990791_m1), GLI1 (Hs00171790_m1), GLI2 (Hs01119974_m1), GLI3 (Hs00609233_m1), TGFβ1 (Hs00998133_m1), TGFβ2 (Hs00234244_m1), TGFβ3 (Hs01086000_m1), FN1 (Hs01549976_m1), COL1A1 (Hs00164004_m1), VCAN (Hs00171642_m1), CTSB (Hs00947433_m1), COMP (Hs00164359_m1), COL11A1 (Hs01097664_m1); GAPDH (Hs027866254_g1) and 18S (Hs03003631_g1), were both used as housekeeping genes (All from Thermo-Fisher Scientific, UK).

Preparation of adipocyte-collagen gels

Purified adipocytes (1ml) were combined with the following reagents to give 0.1w% collagen-adipocyte gels: 1ml of 3mg/ml rat-tail collagen I, 100μl of 10x DMEM low-glucose, 48μl of 1M NaOH and 852μl H_2O, prepared on ice. Adipocyte-gel mixture was incubated at 37°C, 5% CO_2 for 45min in 100μl aliquots in a 96-well dish. Gels were gently transferred to 24-wells and cultured in 1ml Medium-199 with insulin-transferrin-selenium (Gibco). Adipocyte gels were used for experiments with other cell types within 7 days of isolation. For live/dead assays, gels were immersed in 1ml PBS containing 20μg fluorescein diacetate (Sigma-Aldrich) and 4μM ethidium homodimer (Sigma-Aldrich), incubated for 10min at 37°C, then placed on a glass slide with PBS to prevent drying. Gels were imaged using a Zeiss LSM510 confocal microscope.

ELISA

G164 and AOCS were grown in 24-well plates until 70% confluency. After 48h, media was collected, spun down and tested for the presence of TGFβ3 using a TGFβ3 ELISA kit (Abcam 272203).

Preparation of tri-cultures

3D co-cultures of fibroblasts and HGSOC cells were first cultured for 7 days to allow gel contraction and remodeling. Adipocyte gels were placed in dry 24-wells and then using a Pasteur pipette, a co-culture gel with a small volume of media was placed on top of the middle of an adipocyte gel. Co-cultures were embedded into the center of adipocyte gels by carefully pressing down with the curved end of a sterile 1.5ml eppendorf. Wells were then filled with culture media and tri-cultures were allowed to free-float. After 24 hours, ascorbic acid (50μg/ml) was added to gels without or with inhibitors, SB431542 (20μM) and GANT61 (7.5μM). Gel images were acquired before adding factors and at the end of culture (14 days). Media and factors were replenished every 2-3 days and cultured for a further 13 days. At the end point (21 days total culture), tri-cultures were washed well with PBS and fixed in 10% formalin for 2h for IF, or for 24h for paraffin embedding. After fixation, gels were stored in PBS at 4°C until processed.

Immunohistochemistry

FFPE sections (4 μm) of omentum samples or gel-cultures were re-hydrated in ethanol solutions: 100%, 90%, 70%, and finally 50%. Sections were transferred to citric acid-based antigen unmasking solution (Vector Laboratories) and heated in a 2100 antigen-retriever (Aptum Biologics). Sections were treated with 3% H2O2 for 5min and blocked with 5% BSA for 1hr. Primary antibody was added in antibody diluent (Zytomed) for 1hr. Slides were washed and a biotinylated secondary antibody (Vector) was added. Subsequent steps were carried out according to the protocol included with the Vectastain Elite ABC HRP kit. Slides were incubated for 5min with DAB solution made using Sigmafast DAB tablets (Sigma-Aldrich). Finally, slides were counterstained in 50% Gill's hematoxylin I, and dehydrated in 50%, 70%, and 100% ethanol then twice in xylene. Coverslips were affixed using DPX mountant (Sigma-Aldrich). All sections were scanned using a 3DHISTECH Panoramic 250 digital slide scanner (3DHISTECH), and the resulting scans were analyzed using Definiens software (Definiens AG). Disease scores were determined first by manually defining regions of interest in the tissue that represented tumor, stroma, fat (adipocytes), and then training the software to recognize these regions of interest. Disease score was expressed as a percentage of the whole tissue area that contained tumor and/or stroma (Figure 1A).

Immunofluorescence

Gels were fixed overnight in 10% neutral buffered formalin, washed in PBS and permeabilized in Triton X-100 (0.5% in PBS) for 10min. Gels were incubated in blocking solution (5% BSA or goat serum), and then incubated with primary antibody overnight at 4°C. Gels were washed and incubated with fluorescent secondary antibody, for 1hr protected from light and then washed. Finally, gels were incubated with 0.4 μg/ml DAPI and then washed. Fluorescent images of tri-cultures were captured on an inverted Zeiss LSM 510 laser-scanning confocal microscope using a 10x or 20x air objective. Specimen images were acquired with a field of view equal to 238.1 x 238.1μm containing 1024x1024 pixels. All imaging conditions including laser settings and scan settings were kept constant for all gel groups for each fluorescent-labeled antibody. Images of monolayers were captured using an EVOS FLoid Cell Imaging Station. For F-actin, Alexa Fluor 568 Phalloidin (A12380, Thermo Fisher Scientific) was used.

Antibodies

The following antibodies were used for immunostaining: anti-actin, α-smooth muscle (clone 1A4, A2547), anti-VCAN (polyclonal, HPA004726), anti-COL11A1 (polyclonal, HPA052246), anti-COL1A1 (polyclonal, HPA011795), anti-FN1 (polyclonal, F3648) all from Sigma-Aldrich, UK; anti-Ki67 (cloneMIB-1, M7240), from Dako, UK; anti-fibroblast activation protein, alpha (EPR 20021, ab207178), anti-COMP (ab11056), anti-CTSB (CA10, ab58802), anti-TGFβ all from Abcam; anti-PAX8 (NBP1-32440) from Novus; anti-EPCAM Alexa Fluor 488 conjugated (53-8326-41) from Thermo-Fisher; GLI-1 Antibody (C-1, sc-515751) from Santa Cruz Biotechnology.

ICGC analysis for six matrisome molecules

The ICGC_OV read counts across 93 primary tumors were extracted from the exp_seq.OV-AU.tsv.gz file in the ICGC data repository Release 20 (http://dcc.icgc.org). Only genes that achieved at least one read count in at least ten samples were selected, producing 18,010 filtered genes in total. Variance stabilizing transformation was then applied using the rlog function (Love et al., 2014). Overall survival (OS) was extracted from the donor.OV-AU.tsv.gz file. Mean expression for the six matrisome genes was calculated for each sample and high and low matrix groups were determined using the method described previously (Mihaly et al., 2013). Survival modeling and Kaplan-Meier (KM) analysis was undertaken using R package survival. OS was defined as time from diagnosis to death, or to the last follow-up date for survivors. The significantly differentially expressed genes were selected using a false discovery rate (FDR) < 0.05.

RNA-seq and analysis

RNA-seq was performed by the Wellcome Trust Centre for Human Genetics (Oxford, UK) to approximately 30x mean depth for the HGSOC cell lines or 20x for the 3D cultures. The sequencing was carried out on the Illumina HiSeq4000 or on the NovaSeq6000 platform, strand-specific, generating 150bp paired-end reads. RNA-Seq reads were mapped to the human genome (hg19, Genome Reference Consortium GRCh37) in strand-specific mode as part of the Wellcome Trust Centre pipeline. Number of reads aligned to the exonic region of each gene were counted using htseq-count based on the Ensembl annotation (Anders et al., 2014). Only genes that achieved at least one read count per million reads (cpm) in at least twenty-five

percent of the samples were kept. Conditional quantile normalization was performed counting for gene length and GC content and a $\log_2$ transformed RPKM expression matrix was generated. RNA-Seq data have been deposited in Gene Expression Omnibus (GEO) under the accession number GSE125109.

QUANTIFICATION AND STATISTICAL ANALYSIS

Statistical analyses and graphics were performed in GraphPad Prism or the programming language R (version 3.1.3). All correlations were calculated using Spearman's rank correlation. For pairwise comparisons a two-way paired t-test was used. For comparisons of >t2 sample means, one-way ANOVA with Tukey's HSD test were used. Differential expression analysis was performed in Edge R using limma (Ritchie et al., 2015; Subramanian et al., 2005).Gene-set enrichment analysis (GSEA) was performed using the GSEA software (Mootha et al., 2003) to identify the canonical pathways gene sets from the Molecular Signatures Database (MSigDB-C2-CP v6.2). See figure legends for significance levels and number of samples, n. For experiments involving OFs, n represents technical replicates and N represents number of donors. Data were considered statistically significant from $p < 0.05$.